

# Dynamic Evolution of Palladium Single Atoms on Anatase Titania Support Determines the Reverse Water–Gas Shift Activity

Linxiao Chen, Sarah I. Allec, Manh-Thuong Nguyen, Libor Kovarik, Adam S. Hoffman, Jiyun Hong, Debora Meira, Honghong Shi, Simon R. Bare, Vassiliki-Alexandra Glezakou, Roger Rousseau, and János Szanyi\*



Cite This: *J. Am. Chem. Soc.* 2023, 145, 10847–10860



Read Online

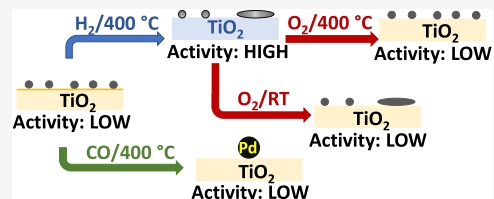
ACCESS |

Metrics & More

Article Recommendations

Supporting Information

**ABSTRACT:** Research interest in single-atom catalysts (SACs) has been continuously increasing. However, the lack of understanding of the dynamic behaviors of SACs during applications hinders catalyst development and mechanistic understanding. Herein, we report on the evolution of active sites over Pd/TiO<sub>2</sub>-anatase SAC (Pd<sub>1</sub>/TiO<sub>2</sub>) in the reverse water–gas shift (rWGS) reaction. Combining kinetics, *in situ* characterization, and theory, we show that at  $T \geq 350$  °C, the reduction of TiO<sub>2</sub> by H<sub>2</sub> alters the coordination environment of Pd, creating Pd sites with partially cleaved Pd–O interfacial bonds and a unique electronic structure that exhibit high intrinsic rWGS activity through the carboxyl pathway. The activation by H<sub>2</sub> is accompanied by the partial sintering of single Pd atoms (Pd<sub>1</sub>) into disordered, flat, ~1 nm diameter clusters (Pd<sub>n</sub>). The highly active Pd sites in the new coordination environment under H<sub>2</sub> are eliminated by oxidation, which, when performed at a high temperature, also redisperses Pd<sub>n</sub> and facilitates the reduction of TiO<sub>2</sub>. In contrast, Pd<sub>1</sub> sinters into crystalline, ~5 nm particles (Pd<sub>NP</sub>) during CO treatment, deactivating Pd<sub>1</sub>/TiO<sub>2</sub>. During the rWGS reaction, the two Pd evolution pathways coexist. The activation by H<sub>2</sub> dominates, leading to the increasing rate with time-on-stream, and steady-state Pd active sites similar to the ones formed under H<sub>2</sub>. This work demonstrates how the coordination environment and nuclearity of metal sites on a SAC evolve during catalysis and pretreatments and how their activity is modulated by these behaviors. These insights on SAC dynamics and the structure–function relationship are valuable to mechanistic understanding and catalyst design.



## INTRODUCTION

The past decade has witnessed the explosion of research on atomically dispersed metal catalysts or “single-atom catalysts (SACs)”. The interest is driven by the desire to reach the high metal utilization efficiency and site uniformity of homogeneous catalysts on durable, process-friendly heterogeneous platforms.<sup>1–3</sup> Extensive efforts delivered significant progress in the areas of synthesis,<sup>4–8</sup> characterization,<sup>9–11</sup> applications,<sup>12–19</sup> and mechanistic insights.<sup>20–22</sup> Despite the advances, an enduring issue haunting related research is the complicated dynamics of SACs. Because single metal atoms are only bound to binding motifs offered by the support, compared to metal nanoparticles, they are often less stable, and their properties are more sensitive to changes in the support and the metal–support interface (MSI).<sup>23–26</sup> As a result, the structural and electronic properties of SACs often respond to the reaction and/or pretreatment conditions drastically, which can profoundly affect catalysis.<sup>21,24,27–29</sup> Understanding these behaviors is necessary for developing stable SACs for applications under harsh conditions, as well as accurately identifying active sites, reaction mechanisms, and the structure–function relationship.

Despite their importance, the dynamics of SACs and their catalytic consequences are often neglected or difficult to reveal.

The characterization of SACs is challenging, and it needs to be conducted *in situ* to accurately correlate it with kinetic data.<sup>9–11</sup> In addition, the “site uniformity” on SACs is more of a wish than reality,<sup>30–32</sup> due to the presence of various binding sites on supports, high mobility of single metal atoms, and changes in the support structure during catalysis.<sup>33–35</sup> Different types of sites and their roles in catalysis are hard to deconvolute as most spectroscopic techniques yield ensemble-average information. Thus, reliable experimental insights about catalyst dynamics, actual active sites, and structure–function relationships on SACs are rare,<sup>17,21,23,24,27–29,36–38</sup> impeding the understanding of reaction chemistry and rational catalyst design.

In this work, we investigated the dynamic structural evolution of a Pd/TiO<sub>2</sub>-anatase SAC and its impacts on the reverse water–gas shift (rWGS) reaction, i.e., CO<sub>2</sub> hydrogenation to CO. The rWGS has sparked significant interests

Received: March 5, 2023

Published: May 5, 2023



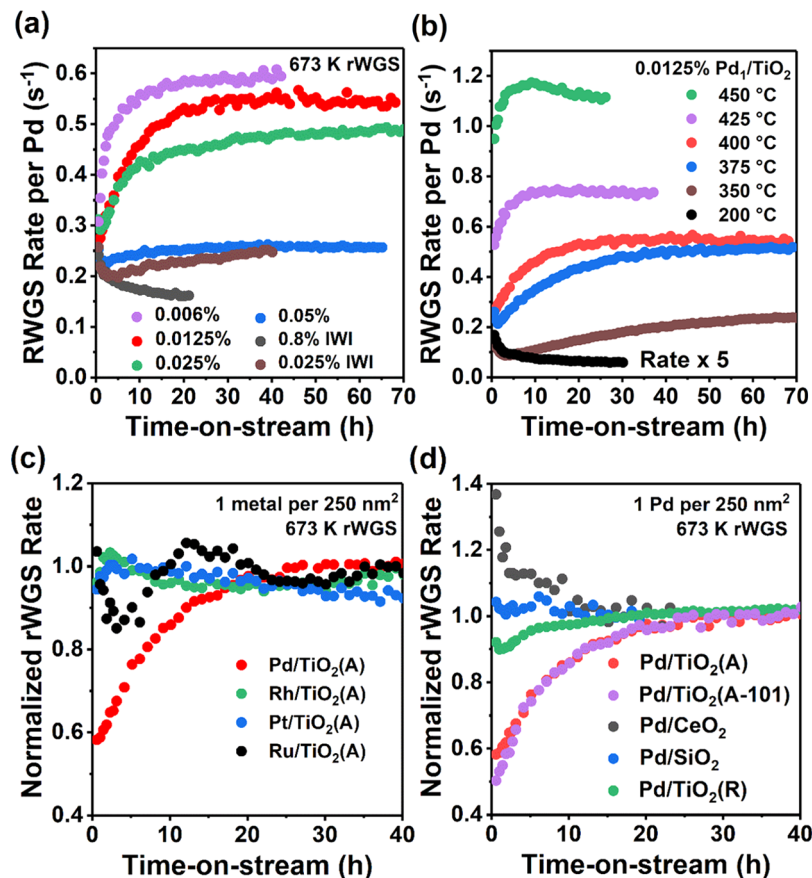


**Figure 1.** Variations in the rWGS rate per Pd with TOS at 400 °C: (a) Pd/TiO<sub>2</sub> of various Pd loadings by wt %: 0.006 (purple), 0.0125 (red), 0.025 (green), 0.05 (blue), 0.025 synthesized by IWI (brown), and 0.8 (IWI, black); (b) 0.0125 wt % Pd<sub>1</sub>/TiO<sub>2</sub> at various temperatures: 450 (green), 425 (purple), 400 (red), 375 (blue), 350 (brown), and 200 °C (black, rate multiplied by 5); (c) (normalized to the final rate) various noble metals supported on anatase TiO<sub>2</sub>: Pd (red), Rh (green), Pt (blue), and Ru (black); (d) (normalized to the final rate) Pd supported on various oxides: anatase (red), anatase with >90% (101) surfaces (purple), CeO<sub>2</sub> (black), SiO<sub>2</sub> (blue), and rutile (green). All catalysts in panels (c) and (d) share the noble metal coverage and synthesis method with 0.0125 wt % Pd<sub>1</sub>/TiO<sub>2</sub>, and near-atomic dispersion is expected (atomic dispersion of Pt/TiO<sub>2</sub> reported).<sup>37</sup> Absolute rates are reported in Table S1. Typical reaction conditions: 50 mg of the catalyst,  $T = 400\text{ }^\circ\text{C}$ , H<sub>2</sub>/CO/He = 4:1:5, total flow = 10 SCCM, 1 atm. The rate on pristine TiO<sub>2</sub> was subtracted.

for both practical and fundamental reasons,<sup>39–43</sup> and mechanistic studies predicted SACs to be ideal for this reaction.<sup>39,44</sup> Combining detailed kinetics, comprehensive in situ characterization, and theoretical modeling, we revealed the formation of Pd sites with high intrinsic activity during the reaction. This is achieved through the reduction of TiO<sub>2</sub> by H<sub>2</sub>, leading to Pd sites with a unique electronic structure and partially cleaved MSI, which are particularly effective in the carboxyl pathway of the rWGS. Oxidation eliminates these highly active Pd sites by reversing these coordination environment changes. In contrast, reducing the SAC with CO leads to severe sintering of single Pd atoms (Pd<sub>1</sub>) and thus the loss of rWGS active sites and, consequently, activity. The comprehensive insights offered by this work on single-atom catalysis are rare in the literature and instructive for the rational design of SACs.

## RESULTS

**Changes in the rWGS Rate on Pd<sub>1</sub>/TiO<sub>2</sub>: Activation by H<sub>2</sub> and Deactivation by CO.** Pd/TiO<sub>2</sub>-anatase SACs (herein referred to as “Pd<sub>1</sub>/TiO<sub>2</sub>”; “TiO<sub>2</sub>” and “TiO<sub>2</sub>-A” both refer to anatase TiO<sub>2</sub>) were synthesized by strong electrostatic adsorption.<sup>7</sup> The atomic dispersion of Pd on 0.0125 wt % (loading verified by ICP) Pd<sub>1</sub>/TiO<sub>2</sub> was confirmed by the

results of high-angle annular dark-field scanning transmission electron microscopy (HAADF-STEM), X-ray absorption spectroscopy (XAS), and CO adsorption IR (CO-IR) measurements, which will be shown later. XAS also shows the atomic dispersion of Pd at ≤0.05 wt % loading (Figure S2). In CO<sub>2</sub> hydrogenation at 400 °C under ambient pressure, all Pd<sub>1</sub>/TiO<sub>2</sub> with different Pd loadings exhibit >99% selectivity toward CO (reverse water–gas shift, rWGS, <10% CO<sub>2</sub> conversion), as expected on highly dispersed noble metal catalysts.<sup>40,45–47</sup> Interestingly, we observed a slow (in ~25 h), gradual, twofold increase in the rWGS rate per Pd with time-on-stream (TOS) on ≤0.025 wt % Pd<sub>1</sub>/TiO<sub>2</sub> (purple, red, and green in Figure 1a). Since anatase is stable at 400 °C,<sup>48</sup> the rate increase is not caused by the support phase change. Since Pd is atomically dispersed on fresh Pd<sub>1</sub>/TiO<sub>2</sub>, the rate increase cannot be due to higher Pd dispersion, i.e., more peripheral Pd sites that contribute to the majority of the rWGS activity,<sup>39,44</sup> either. Therefore, it reflects higher intrinsic activity of Pd. In contrast, less dispersed Pd/TiO<sub>2</sub>, synthesized by incipient wetness impregnation (0.025 or 0.8 wt % Pd), or 0.05 wt % Pd<sub>1</sub>/TiO<sub>2</sub> do not show the phenomenon (brown, black, and blue symbols, respectively, in Figure 1a; dilution with pristine TiO<sub>2</sub> has no effect, Figure S3), indicating that the increase in intrinsic activity can only be observed when Pd is highly, if not

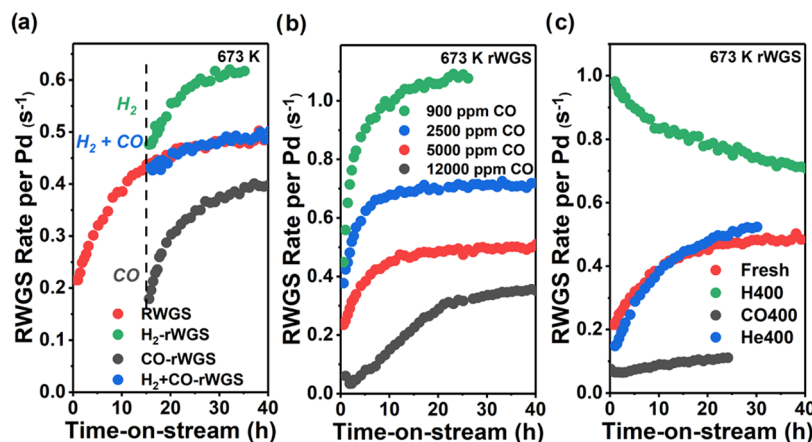


**Figure 2.** Variations in the rWGS rate per Pd with TOS at 400 °C on 0.0125 wt % Pd<sub>1</sub>/TiO<sub>2</sub>, showing the effects of H<sub>2</sub> and CO: (a) Pd<sub>1</sub>/TiO<sub>2</sub> in the first 15 h under the rWGS stream (red, 40% H<sub>2</sub>, 10% CO<sub>2</sub>, ~5% CO<sub>2</sub> conversion), 40% H<sub>2</sub> (green), 5000 ppm CO (black), and 40% H<sub>2</sub> + 5000 ppm CO (blue) at 400 °C; (b) with various CO concentrations in the rWGS stream: 900 (green, 5 mg of the catalyst), 2500 (blue, 20 mg of the catalyst), 5000 (red), and 12,000 ppm (CO, 10,000 ppm CO added); (c) after pretreating Pd<sub>1</sub>/TiO<sub>2</sub> with no treatment (red), 40% H<sub>2</sub> at 400 °C for 40 h (green), 5% CO at 400 °C for 24 h (black), and He at 400 °C for 24 h (blue). Typical reaction conditions are identical with Figure 1.

atomically dispersed and at very low surface coverage (1 Pd<sub>1</sub> per ~120 nm<sup>2</sup> TiO<sub>2</sub> surface at 0.025 wt % loading).

To understand the intrinsic activity increase, we tested the rWGS on 0.0125 wt % Pd<sub>1</sub>/TiO<sub>2</sub> (used in all experiments below) at various temperatures. Figure 1b shows that the rate increases with TOS at  $T \geq 350$  °C, but at 350 (brown) and 375 °C (blue), it drops first before it increases. In contrast, at 200 °C (black), the rate decreases monotonically with TOS, presumably due to sintering. Thus, the activation of Pd<sub>1</sub>/TiO<sub>2</sub> requires high temperature, consistent with its high apparent activation barrier of ~120 kJ/mol (Figure S4, obtained by modeling data in Figure 1b). We also tested Pd/CeO<sub>2</sub>, Pd/SiO<sub>2</sub>, Pd/TiO<sub>2</sub>-rutile (“TiO<sub>2</sub>-R”), Pt/TiO<sub>2</sub> (atomically dispersed<sup>37</sup>), Rh/TiO<sub>2</sub>, and Ru/TiO<sub>2</sub>, with the same synthesis procedure and noble metal coverage consistent with 0.0125 wt % Pd<sub>1</sub>/TiO<sub>2</sub>. Figure 1c,d shows that none of the other highly dispersed M/M'<sub>x</sub>O<sub>y</sub> catalysts show an increasing rate with TOS, i.e., the intrinsic activity increase is unique to Pd<sub>1</sub>/TiO<sub>2</sub>-A, implying that it involves a specific metal–support interaction. Particularly, the absence of the phenomenon on CeO<sub>2</sub> and TiO<sub>2</sub>-R, on which surface oxygen vacancies (O<sub>v</sub>) are more favored than on TiO<sub>2</sub>-A,<sup>49–52</sup> suggests that it is not due to surface O<sub>v</sub> directly participating in the rWGS. Note that we also tested Pd on a faceted TiO<sub>2</sub>-A with >90% exposed surfaces as (101) orientation, the most stable surface of anatase (see Figure S5 for TEM images).<sup>51,53–55</sup> It exhibits an identical rate trend (purple in Figure 1d) with Pd<sub>1</sub>/TiO<sub>2</sub> (red), indicating that the (101) surface is an appropriate model for TiO<sub>2</sub>-A for the theoretical modeling study below.

The rWGS stream exiting the reactor comprises of 40% H<sub>2</sub>, 10% CO<sub>2</sub>, and ~5000 ppm CO and H<sub>2</sub>O (from ~5% CO<sub>2</sub> conversion). As a first step to reveal the physical origin of the intrinsic activity increase, the effects of each component of the gas stream were deconvoluted. In the first 15 h, we replaced the rWGS stream with 40% H<sub>2</sub>, 5000 ppm CO, or 40% H<sub>2</sub> + 5000 ppm CO at 400 °C (H<sub>2</sub> and CO concentrations equal to those in the rWGS stream), and switched to the rWGS stream at  $t = 15$  h. Figure 2a shows that the H<sub>2</sub> + CO mixture (blue) has an identical impact on the activity of Pd<sub>1</sub>/TiO<sub>2</sub> with the rWGS stream (red). In comparison, Pd<sub>1</sub>/TiO<sub>2</sub> becomes more active under H<sub>2</sub> alone (green) and less active under CO alone (black). The results imply that H<sub>2</sub> causes the intrinsic activity

increase, while CO deactivates the catalyst. During the rWGS, H<sub>2</sub> and CO function in parallel. Thus, H<sub>2</sub> + CO in He exactly replicates the effects of the rWGS stream, and we deduce that H<sub>2</sub>O and CO<sub>2</sub> in the reaction stream have no or minimal effects. To verify this observation, we varied the CO concentration in the rWGS stream either by adding CO or by reducing the amount of catalyst and thus CO<sub>2</sub> conversion. Figure 2b shows that the final per-Pd rate is negatively correlated with CO concentration, supporting the deactivating effect of CO. In addition, we pretreated Pd<sub>1</sub>/TiO<sub>2</sub> with H<sub>2</sub> or CO at 400 °C (referred to as “H400” and “CO400” Pd<sub>1</sub>/TiO<sub>2</sub>, respectively, with higher concentration and/or time to ensure the complete evolution of Pd). Figure 2c shows that the initial rate on H400 Pd<sub>1</sub>/TiO<sub>2</sub> (green) is higher than the final rate on the fresh catalyst (red), and the rate drops with TOS when the rWGS stream, and thus CO, is introduced. In contrast, CO400 Pd<sub>1</sub>/TiO<sub>2</sub> (black) shows a lower initial rate and minimal rate increase compared to the fresh catalyst. The results further verify that H<sub>2</sub> and CO activate and deactivate Pd<sub>1</sub>/TiO<sub>2</sub>, respectively. When CO concentration is very low (green in Figure 2b), i.e., the deactivation by CO is negligible, the final rate on fresh Pd<sub>1</sub>/TiO<sub>2</sub> is close to the initial rate on H400 Pd<sub>1</sub>/TiO<sub>2</sub> (green in Figure 2c, both ~1.0 s<sup>-1</sup> per Pd), as predicted by our conclusion. We note that in Figure 2c, 400 °C He treatment (blue) has no effects on the rWGS rate, eliminating the possibility that the activation is caused by the dehydroxylation of TiO<sub>2</sub> surfaces. Since the effects of the rWGS stream on the structure and activity of Pd are a combination of the effects of H<sub>2</sub> and CO, we will mostly focus on the characterization of fresh, H400, and CO400 Pd<sub>1</sub>/TiO<sub>2</sub>, to understand the physical origins of these observations.

**Dynamic Coordination Environment and Metal Nuclearity in Pd<sub>1</sub>/TiO<sub>2</sub> under H<sub>2</sub> and CO.** The nuclearity of Pd was evaluated by STEM, with results summarized in Figure 3. The fresh catalyst has exclusively Pd<sub>1</sub> (Figure 3a), with no signs of Pd aggregates. The atomic dispersion of Pd is supported by CO-IR, which only shows the 2112 cm<sup>-1</sup> band from CO linearly adsorbed on the cationic Pd (Figure S1, fwhm  $\approx$  20 cm<sup>-1</sup>, suggesting nonuniform environments of Pd<sub>1</sub>),<sup>27,56–59</sup> with no bridging CO on the adjacent Pd sites (1800–2000 cm<sup>-1</sup>). On the H400 catalyst, both Pd<sub>1</sub> (Figure 3b) and Pd aggregates of  $d = 1.2 \pm 0.3$  nm (Figure 3c) were

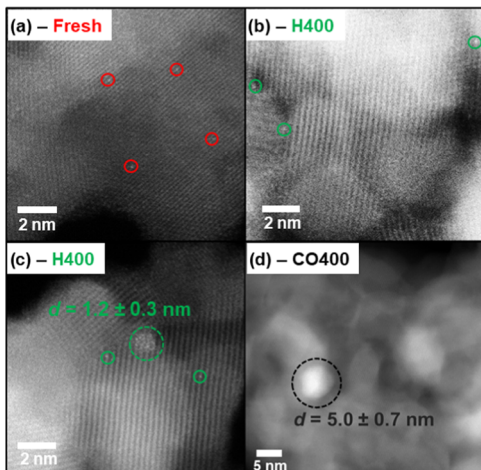


**Figure 3.** HAADF-STEM images of 0.0125 wt%  $\text{Pd}_1/\text{TiO}_2$ : (a) representative image of the fresh sample, with only  $\text{Pd}_1$  (in red circle) found; (b, c) two types of representative images of the H400 sample (transferred immediately into the vacuum after the treatment), one with only  $\text{Pd}_1$  (in green circle) and another with  $\text{Pd}_{\text{n}}$  of  $d = 1.2 \pm 0.3 \text{ nm}$  (in green dashed circle) found; (d) representative image of the CO400 sample, with only  $\text{Pd}_{\text{NP}}$  of  $d = 5.0 \pm 0.7 \text{ nm}$  (in black dashed circles) found. Additional images are included in Figures S6–7 to show the representativeness of the images and the lack of electron-beam artifacts.

identified, indicating that a fraction of  $\text{Pd}_1$  sinters into small Pd clusters (“ $\text{Pd}_{\text{n}}$ ”) under  $\text{H}_2$ . These  $\text{Pd}_{\text{n}}$  do not exhibit a well-defined three-dimensional (3D) structure, and instead, are flattened plates, suggested by their low contrast with  $\text{TiO}_2$ , and appear to be disordered. Meanwhile, CO adsorption on H400  $\text{Pd}_1/\text{TiO}_2$  yields a broad IR band between 2100 and 2040  $\text{cm}^{-1}$  from linear CO on various surface sites on Pd aggregates (Figure S1),<sup>56–59</sup> along with the 2114  $\text{cm}^{-1}$  linear CO on the  $\text{Pd}^{m+}$  peak, supporting the partial sintering of  $\text{Pd}_1$  into  $\text{Pd}_{\text{n}}$ . In contrast, on the CO400 catalyst, only large Pd nanoparticles of  $d = 5.0 \pm 0.7 \text{ nm}$  (“ $\text{Pd}_{\text{NP}}$ ”) were identified, with no  $\text{Pd}_1$ , suggesting complete, severe  $\text{Pd}_1$  sintering under CO. These  $\text{Pd}_{\text{NP}}$  have very bright contrast compared to  $\text{TiO}_2$ , and Pd lattice diffraction can be observed (Figure S6d), indicating that unlike  $\text{Pd}_{\text{n}}$ , they are three-dimensional and crystalline.

The local coordination environment and oxidation state of Pd sites were examined by in situ Pd K-edge XAS, with results summarized in Figure 4 and Table 1. For fresh  $\text{Pd}_1/\text{TiO}_2$ , the best model to fit its extended X-ray absorption fine structure (EXAFS) between 1 and 4 Å includes a Pd–O single scattering path at 2.00 Å, a bonding distance, a Pd–Ti single scattering path at 2.95 Å, a nonbonding next-neighbor interaction, and a Pd–O single scattering path at 3.87 Å, a next-next-neighbor interaction (red in Figure 4a and Table 1). Replacing the Pd–Ti path with a Pd–Pd path led to poor agreement with the data between 2 and 3 Å (Figure S8a). Therefore, we deduce that the EXAFS of fresh  $\text{Pd}_1/\text{TiO}_2$  has negligible contribution from Pd–Pd, further confirming that the Pd is predominantly atomically dispersed, and the average coordination number ( $N$ ) of  $\text{Pd}_1$  with the nearest O ( $R \approx 2.00 \text{ \AA}$ ) is  $3.2 \pm 0.4$  (Table 1). In the X-ray absorption near-edge spectroscopy (XANES) region (Figure 4b), the white-line intensity, the energy at which the edge starts to increase (edge onset energy), and the edge line shapes of fresh  $\text{Pd}_1/\text{TiO}_2$  (red) are all similar with those of  $\text{PdO}$  (cyan), indicating that the oxidation state of fresh  $\text{Pd}_1$  is close to  $\text{Pd}(\text{II})$ .

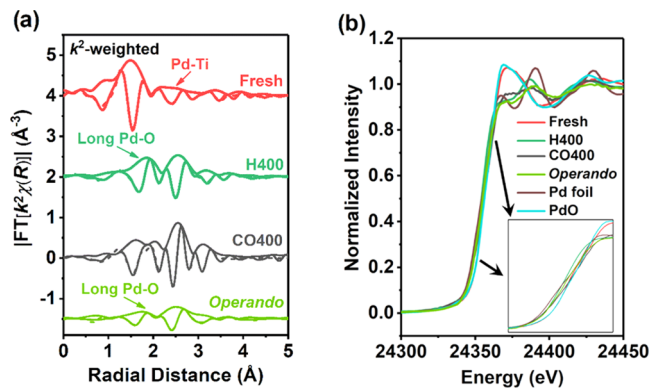


**Figure 4.** Pd K-edge XAS results on 0.0125 wt %  $\text{Pd}_1/\text{TiO}_2$ : (a) EXAFS (R-space magnitude and imaginary part, best fitting shown as dashed curves, raw  $\chi$  data shown in Figure S8c) and (b) XANES (the inset magnifying the edge). Red, green, and black curves represent the fresh, H400 (collected in situ), and CO400 (collected ex situ after air exposure) catalysts, respectively. The light green curves represent data collected operando at the steady state ( $450 \text{ }^{\circ}\text{C}$ , 5%  $\text{H}_2$ ). Brown and cyan curves represent Pd foil and  $\text{PdO}$  standards. The EXAFS fitting parameters are listed in Table 1.

After activation with  $\text{H}_2$ , a Pd–Pd scattering path appears in the EXAFS (green in Figure 4a,  $\sim 2.4 \text{ \AA}$  in the  $k^2$ -weighted plot), consistent with the formation of  $\text{Pd}_{\text{n}}$ . The mean square deviation in half-path-length of the Pd–Pd path ( $\sigma^2 = 0.015 \pm 0.001$ ) is much higher than the normal values for the crystalline Pd at the same temperature (e.g.,  $0.005 \pm 0.001$  for Pd foil, Table S2), implying high disorder in the Pd–Pd bonds, echoing with  $\text{Pd}_{\text{n}}$  appearing disordered in STEM. If  $\text{Pd}_{\text{n}}$  were of hemispherical shape, the  $N(\text{Pd–Pd}_1)$ , i.e., the coordination number of directly bonded Pd–Pd, value of  $6.8 \pm 0.6$  on H400  $\text{Pd}_1/\text{TiO}_2$  (Table S2) would predict  $N(\text{Pd–Pd}_2) \approx 3.2$ .<sup>60</sup> The actual  $N(\text{Pd–Pd}_2) = 1.6 \pm 0.4$  (Table 1) is lower than the predicted value assuming hemispherical shape, indicating that  $\text{Pd}_{\text{n}}$  are flattened, consistent with the low contrast in STEM (Figure 3c). Interestingly, most direct Pd–O bonds on H400  $\text{Pd}_1/\text{TiO}_2$  are significantly longer than normal Pd–O bonds ( $2.533 \pm 0.007$  compared to  $2.00 \pm 0.01 \text{ \AA}$  on the fresh sample, Table 1). Such long M–O bonds on  $\text{H}_2$ -reduced metal-oxide catalysts have been previously reported<sup>61–67</sup> and suggest that the  $\text{Pd}/\text{TiO}_2$  interface is partially cleaved by  $\text{H}_2$ -reduction. Such a cleavage could be a result of the hydroxylation of the interface, as previous works and theoretical calculation suggested.<sup>39,62,68,69</sup> We note that the EXAFS oscillations resulting from the long Pd–O path cannot be from Pd–Ti scattering, as its imaginary part is out of phase with Pd–Ti (Figure S8b), and thus cannot be properly fit with a model replacing the long Pd–O path with a Pd–Ti path. Meanwhile, in the XANES region (Figure 4b), the white-line intensity of H400  $\text{Pd}_1/\text{TiO}_2$  (green) is slightly lower than that of the Pd foil (brown), and both the edge onset energy and the edge line shape are obviously different (inset showing the zoom-in view of the edge), suggesting that the electronic structure of Pd sites on H400  $\text{Pd}_1/\text{TiO}_2$  is different from that of regular metallic Pd.

The EXAFS of CO400  $\text{Pd}_1/\text{TiO}_2$  is dominated by Pd–Pd scattering between 2.4 and 3.5 Å (black in Figure 4a). Even though this sample was measured after air exposure, most of the Pd appears to be metallic (Pd–Pd scattering path at  $R = 2.75 \pm 0.02 \text{ \AA}$ , Table 1), and in the XANES region (Figure 4b), both the white-line intensity and the edge line shape

**Table 1.** Fitting Parameters from the Best EXAFS Models of 0.0125 wt % Pd<sub>13</sub>/TiO<sub>2</sub><sup>a</sup>

catalyst status	fresh	H400	CO400 (ex situ)	operando
<i>k</i> range (Å <sup>-1</sup> )	3–9.6			
<i>R</i> range (Å)	1–4			
<i>S</i> <sub>o</sub> <sup>2</sup>	0.82			0.75
Δ <i>E</i> <sub>o</sub> (eV)	1 (1)	-7.2 (6)	3 (1)	-4 (1)
Pd–O (bonding, normal)	<i>N</i>	3.2 (4)	0.4	1.1 (6)
	<i>R</i> (Å)	2.00 (1)	2.13 (4)	1.99 (3)
	<i>σ</i> <sup>2</sup>	0.003 (1)	0.005	0.004 (2)
Pd–O (bonding, long)	<i>N</i>	N/A	2.7 (3)	N/A
	<i>R</i> (Å)		2.533 (7)	2.41 (3)
	<i>σ</i> <sup>2</sup>		0.005	0.013
Pd–Pd (metallic, bonding)	<i>N</i>	N/A	6.8 (6)	5 (1)
	<i>R</i> (Å)		2.761 (6)	2.75 (2)
	<i>σ</i> <sup>2</sup>		0.015 (1)	0.009 (3)
Pd–Ti (nonbonding)	<i>N</i>	1.2 (3)	N/A	N/A
	<i>R</i> (Å)	2.95 (3)		
	<i>σ</i> <sup>2</sup>	0.007		
Pd–Pd (oxide)	<i>N</i>	N/A	N/A	0.7 (5)
	<i>R</i> (Å)			3.02 (7)
	<i>σ</i> <sup>2</sup>			0.004
Pd–Pd (oxide)	<i>N</i>	N/A	N/A	1.4 (7)
	<i>R</i> (Å)			3.41 (3)
	<i>σ</i> <sup>2</sup>			0.004
Pd–O (next-next-neighbor)	<i>N</i>	7 (2)	N/A	N/A
	<i>R</i> (Å)	3.87 (3)		
	<i>σ</i> <sup>2</sup>	0.012		
Pd–Pd (metallic, next-next-neighbor)	<i>N</i>	N/A	1.6 (4)	N/A
	<i>R</i> (Å)		3.83 (2)	3.75 (4)
	<i>σ</i> <sup>2</sup>		0.008	0.012

<sup>a</sup>Numbers in brackets are fitting standard deviations of the last digit. *S*<sub>o</sub><sup>2</sup> was determined by fitting the EXAFS of the Pd foil. Two paths were used to represent Pd–Pd scattering in the oxide form based on the structure of PdO. Operando data were collected at 450 °C, while others were collected at room temperature at a different beamline, leading to different *σ*<sup>2</sup> and *S*<sub>o</sub><sup>2</sup> values. H<sub>2</sub> treatment was performed at 450 °C to expedite the experiment.

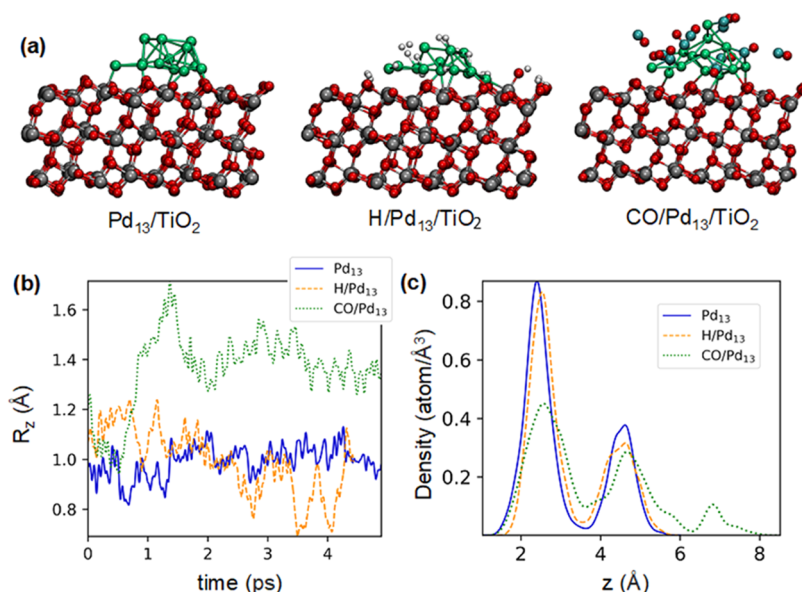


**Figure 5.** (a) Final geometries of the three simulated systems (color codes: O in red, Ti in gray, Pd in lime, C in cyan, and H in dark white); (b) *R*<sub>z</sub>(*t*) for Pd<sub>13</sub>/TiO<sub>2</sub>, H/Pd<sub>13</sub>/TiO<sub>2</sub>, and CO/Pd<sub>13</sub>/TiO<sub>2</sub>; and (c) Pd density as a function of the distance from the TiO<sub>2</sub> surface.

resemble those of the Pd foil (black compared to brown). In addition, *σ*<sup>2</sup>(Pd–Pd) values ( $0.009 \pm 0.003$  and  $0.004$  for metallic and oxide paths) are normal for the crystalline Pd. These characteristics suggest that after the CO treatment, most

Pd<sub>1</sub> agglomerate into crystalline, metallic Pd<sub>NP</sub> stable under room-temperature air, consistent with the STEM images showing the three-dimensional crystalline Pd<sub>NP</sub>. In summary, the combination of STEM, XAS, and CO-IR revealed that

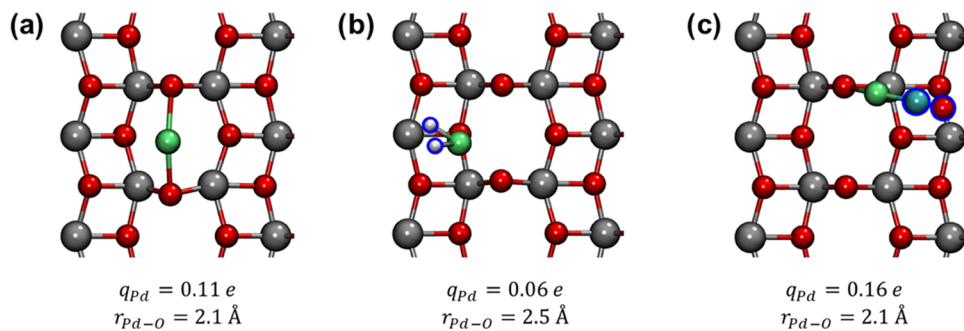


**Figure 6.** Top view of the optimized geometries and corresponding Bader charges  $q_{Pd}$  of Pd<sub>1</sub> and Pd–O bond length  $r_{Pd-O}$  of (a) Pd<sub>1</sub>/TiO<sub>2</sub>(101); (b) H<sub>2</sub>-Pd<sub>1</sub>/TiO<sub>2</sub>(101); and (c) CO-Pd<sub>1</sub>/TiO<sub>2</sub>(101). Color codes: O in red, Ti in gray, Pd in lime, C in cyan, and H in dark white. Adsorbate atoms (CO and H) are highlighted in blue.

under H<sub>2</sub>, some Pd<sub>1</sub> form small, disordered, flattened Pd<sub>n</sub> plates, while under CO, all Pd<sub>1</sub> form large, crystalline, three-dimensional Pd<sub>NP</sub>. Also, the H<sub>2</sub>-reduction of Pd<sub>1</sub>/TiO<sub>2</sub> creates elongated Pd–O bonds, i.e., partially cleaved MSI, and Pd sites with distinct electronic structures from the metallic Pd.

XAS was also collected operando when the reaction starting from fresh Pd<sub>1</sub>/TiO<sub>2</sub> reaches the steady state, i.e., rate plateau. The EXAFS (light green in Figure 4a) shows that most Pd–O bonds are elongated to  $R = 2.41 \pm 0.03$  Å (Table 1), and small, flattened, and disordered Pd<sub>n</sub> ( $N(Pd-Pd_1) = 8 \pm 2$ , corresponding with  $d \sim 1.5$  nm;  $N(Pd-Pd_2) = 1.2 \pm 0.7$ , compared to the predicted value from the hemisphere shape 4,  $\sigma^2 = 0.023 \pm 0.003$ ) are formed. Meanwhile, the XANES (light green in Figure 4b) shows a significantly different electronic structure of Pd from metallic, with slightly lower white-line intensity. All XAS characteristics at the steady state resemble those of H400 Pd<sub>1</sub>/TiO<sub>2</sub>, suggesting that active Pd sites formed on Pd<sub>1</sub>/TiO<sub>2</sub> in operando conditions are similar with the highly active ones formed under H<sub>2</sub>, as implied by Figure 2. In the operando-treated catalyst, the length of the Pd–O bond is slightly shorter and the fraction of them in all Pd–O is lower (69% compared to 90%) than those on H400 Pd<sub>1</sub>/TiO<sub>2</sub> due to lower H<sub>2</sub> concentration used (5% compared to 20%), while the slightly larger Pd<sub>n</sub> size could reflect the effect of trace (~1000 ppm) CO.

The effects of H<sub>2</sub> and CO treatments on the structure of Pd/TiO<sub>2</sub> were further examined by atomistic simulations. First, we performed ab initio molecular dynamics (AIMD) simulations of a Pd<sub>13</sub> cluster on anatase TiO<sub>2</sub>(101) (Pd<sub>13</sub>/TiO<sub>2</sub>) in the presence of H atoms and CO molecules, separately, to compare the morphology of Pd aggregates formed under H<sub>2</sub> and CO. At the start of the simulation, 32 H atoms or 16 CO molecules were placed randomly on the TiO<sub>2</sub> surface and on the Pd<sub>13</sub> aggregate. During the simulation, five H<sub>2</sub> molecules and four CO molecules desorbed, respectively. Pd<sub>13</sub>/TiO<sub>2</sub> without adsorbates was also simulated for comparison. The final equilibrated geometries of all simulated systems are shown in Figure 5a. To quantify the dimensionality of the Pd<sub>13</sub> cluster over time, we tracked the z coordinate of the Pd atoms relative to the cluster's center of mass via the following equation

$$R_z(t) = \sqrt{\frac{\sum_{i=1}^{N_{Pd}} (r_z^i(t) - \bar{R}_z(t))^2}{N_{Pd}}}$$

where  $r_z^i(t)$  is the z coordinate of the  $i$ th Pd atom at time  $t$ ,  $\bar{R}_z(t)$  is the center of mass of all Pd atoms at time  $t$ , and  $N_{Pd}$

the number of Pd atoms (13).  $R_z(t)$  was plotted for all three systems in Figure 5b. We observe that the Pd<sub>13</sub> center of mass distribution in the CO-Pd<sub>13</sub>/TiO<sub>2</sub> system is consistently higher than that in the Pd<sub>13</sub>/TiO<sub>2</sub> and H-Pd<sub>13</sub>/TiO<sub>2</sub> systems, indicating that in the presence of CO, the Pd atoms, on average, are more likely to be found farther away from the TiO<sub>2</sub> surface than they are in the presence of H or for the neat system. We also plotted the density of Pd atoms as a function of distance from the TiO<sub>2</sub> surface in Figure 5c, where the density was taken over the entire AIMD trajectories. In this case, we observe similar atomic density distributions for Pd<sub>13</sub>/TiO<sub>2</sub> and H-Pd<sub>13</sub>/TiO<sub>2</sub> systems with two major peaks, which indicate that the Pd<sub>13</sub> cluster is mostly organized in two layers. In the case of CO-Pd<sub>13</sub>/TiO<sub>2</sub>, however, we observe three peaks indicative of an emerging third layer and thus, overall, a more three-dimensional structure of the Pd<sub>13</sub> cluster. The AIMD results are consistent with the experimental observations of flattened Pd plates on H400 and three-dimensional Pd particles on CO400 Pd<sub>1</sub>/TiO<sub>2</sub>.

Meanwhile, to examine the changes in the coordination environment of Pd on Pd<sub>1</sub>/TiO<sub>2</sub> under H<sub>2</sub>, we performed density functional theory (DFT) calculations on Pd<sub>1</sub>/TiO<sub>2</sub> with and without adsorbed H atoms. In agreement with Jin et al.,<sup>70</sup> our calculations show that without adsorbates, the most stable adsorption site for Pd<sub>1</sub> on the anatase TiO<sub>2</sub>(101) surface is the OO site, where the Pd atom bridges two twofold coordinated oxygen atoms (O<sub>2C</sub>), as shown in Figure 6a, with the average Pd–O bond length  $r_{Pd-O}$  of 2.1 Å for the nearest O neighbors. The calculated  $r_{Pd-O}$  matches the  $R(Pd-O_1)$  on fresh Pd<sub>1</sub>/TiO<sub>2</sub> from the EXAFS fitting (Table 1), while the apparent difference in the nearest Pd–O coordination number is likely due to O<sub>2</sub> adsorption on the sample. Several different adsorption sites for CO and H<sub>2</sub> on Pd<sub>1</sub>/TiO<sub>2</sub> were tested and the most stable configurations for H<sub>2</sub>-Pd<sub>1</sub>/TiO<sub>2</sub> and CO-Pd<sub>1</sub>/TiO<sub>2</sub> are shown in Figure 6b,c respectively. Upon the adsorption of H<sub>2</sub>, Pd<sub>1</sub> moves from the OO site to a neighboring OTi site. The average  $r_{Pd-O}$  were computed, together with the Bader charge on Pd,  $q_{Pd}$  for Pd<sub>1</sub>/TiO<sub>2</sub> and all H<sub>2</sub>-Pd<sub>1</sub>/TiO<sub>2</sub> and CO-Pd<sub>1</sub>/TiO<sub>2</sub> configurations. Below each structure in Figure 6, we show  $q_{Pd}$  and  $r_{Pd-O}$  for the most stable configurations (complete results are shown in Figure S11a). It is clear that H<sub>2</sub> adsorption significantly increases  $r_{Pd-O}$  from 2.1 to 2.5 Å and decreases  $q_{Pd}$  i.e., increases the electron density on Pd<sub>1</sub>. Therefore, the results of DFT calculations confirm the conclusions of the EXAFS analysis, i.e., H<sub>2</sub> treatment changes the coordination environment of Pd in a way that elongates the Pd–O interfacial bonds to ~2.5 Å

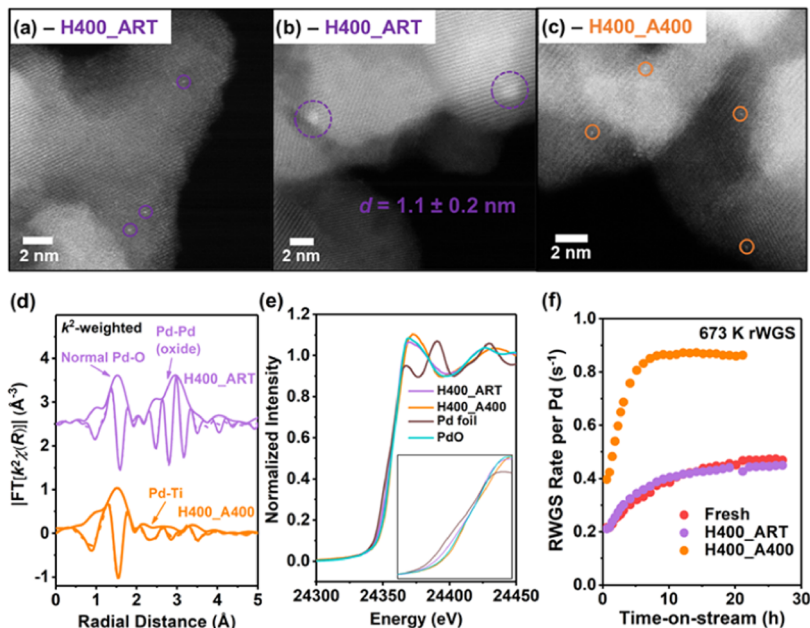


**Figure 7.** Characterization and kinetic results on H400 Pd<sub>1</sub>/TiO<sub>2</sub> oxidized at room temperature (purple, H400\_ART) and 400 °C (orange, H400\_A400): (a, b) two types of representative images of the H400\_ART sample, one with only Pd<sub>1</sub>, and another with Pd clusters of  $d = 1.1 \pm 0.2$  nm found; (c) representative image of the H400\_A400 sample, with only Pd<sub>1</sub> found; (d, e) EXAFS (R-space magnitude and imaginary part, best fitting shown as dashed curves, raw  $\chi$  data shown in Figure S8c) and XANES (the inset magnifying the edge) of the two samples, respectively. The EXAFS fitting parameters are listed in Table S2; brown and cyan curves in panel (e) represent the Pd foil and PdO standard as references. The oxidation in XAS measurements was performed with 20% O<sub>2</sub> in He instead of air; and (f) variations in the rWGS rate per Pd with TOS under identical conditions with Figure 1.

and modifies the electronic structure of Pd, while CO treatment has no such effects.

**H<sub>2</sub>-Induced High Intrinsic Activity of Pd Due to Changes in the Coordination Environment.** Characterization results above offer a clear, logical explanation to the deactivation by CO: the severe sintering of Pd<sub>1</sub> decreases the number of active sites. Nonetheless, the origin of the activation by H<sub>2</sub> remains unsettled, as under H<sub>2</sub>, both the nuclearity (minor sintering) and coordination environment (partial MSI cleavage and electronic structure modification) of Pd change. The effects of the two were deconvoluted by analyzing a H400 Pd<sub>1</sub>/TiO<sub>2</sub> sample exposed to room-temperature air for 2 months (“H400\_ART”). STEM shows that H400\_ART Pd<sub>1</sub>/TiO<sub>2</sub> has similar nuclearity with H400 Pd<sub>1</sub>/TiO<sub>2</sub>, i.e., a mixture of Pd<sub>1</sub> (Figure 7a) and small Pd clusters (Figure 7b) of  $d = 1.1 \pm 0.2$  nm (close to  $d = 1.2 \pm 0.3$  nm in Figure 3c). The similar nuclearity on the two samples is further supported by the similar  $N(\text{Pd-Pd}_1)$  in the EXAFS:  $6.8 \pm 0.6$  (Table 1) compared to  $7 \pm 1$  (Table S2). Meanwhile, the EXAFS also suggests that the direct Pd–O bonds on H400\_ART Pd<sub>1</sub>/TiO<sub>2</sub> (purple in Figure 7d) are of normal length ( $R = 1.99 \pm 0.01$  Å, Table S2) instead of the elongated  $R = 2.533 \pm 0.007$  Å on H400 Pd<sub>1</sub>/TiO<sub>2</sub>. In the XANES region (Figure 7e), both the white-line intensity and the edge onset energy of H400\_ART Pd<sub>1</sub>/TiO<sub>2</sub> (purple) resemble those of PdO (cyan), rather than Pd foil (brown), suggesting Pd<sup>2+</sup> sites instead of the electron-rich Pd sites on H400 Pd<sub>1</sub>/TiO<sub>2</sub>. Therefore, we conclude that the room-temperature oxidation reverses the changes in the Pd coordination environment under H<sub>2</sub> but does not reverse the changes in the Pd nuclearity.

In the rWGS (Figure 7f), H400\_ART Pd<sub>1</sub>/TiO<sub>2</sub> (purple) exhibits identical behaviors with the fresh (red) catalyst, in contrast to the H400 catalyst that shows a high but decreasing

rate (green in Figure 1c). This directly proves that the H<sub>2</sub>-induced high intrinsic activity is due to the changes in Pd coordination environment, i.e., partial MSI cleavage and the unique electronic structure instead of the formation of Pd<sub>n</sub>. This conclusion is further supported by the following observations. First, the activation by H<sub>2</sub> requires >15 h at  $\geq 350$  °C, while the sintering occurs at 200 °C in 3 h (Figure 1b). In fact, operando XAS during the induction period on fresh Pd<sub>1</sub>/TiO<sub>2</sub> indicates a similar level of sintering ( $N(\text{Pd-Pd}_1) = 8 \pm 4$ , Table S2) compared to the steady state but incomplete MSI cleavage of 41% compared to 69% of elongated Pd–O bonds and electronic-state modification (XANES in Figure S9b). Second, the final rate on Pd<sub>1</sub>/TiO<sub>2</sub> increases monotonically when Pd<sub>1</sub> coverage decreases (Figure 1a). Third, treating Pd<sub>1</sub>/TiO<sub>2</sub> at a steady state with He leads to a decrease in the rate, which is recovered quickly by reinitiating the rWGS (Figure S12a). Meanwhile, XAS suggests that the He treatment does not disintegrate Pd<sub>n</sub> (Table S2) but increases the white-line intensity to a level close to metallic Pd (Figure S12b). The change in the Pd electronic state under He is reversed by reinitiating the rWGS (Figure S12b), consistent with the observed rate change. It is likely caused by the desorption of \*H.

**High-Temperature Oxidation Redisperses Pd<sub>n</sub>, Facilitating the rWGS and TiO<sub>2</sub> Reduction.** We previously reported that small, flat, and disordered Pt<sub>n</sub> can be redispersed into Pt<sub>1</sub> by oxidation at room temperature,<sup>37</sup> but Figure 7 shows that Pd<sub>n</sub>, despite having a similar structure with Pt<sub>n</sub>, are only oxidized but not redispersed. Therefore, we attempted to redisperse Pd<sub>n</sub> on H400 Pd<sub>1</sub>/TiO<sub>2</sub> by oxidation at 400 °C in air (“H400\_A400”). Figure 7 shows that H400\_A400 Pd<sub>1</sub>/TiO<sub>2</sub> only has Pd<sub>1</sub> in STEM (Figure 7c), and its EXAFS (orange in Figure 7d and Table S2) resembles that of fresh

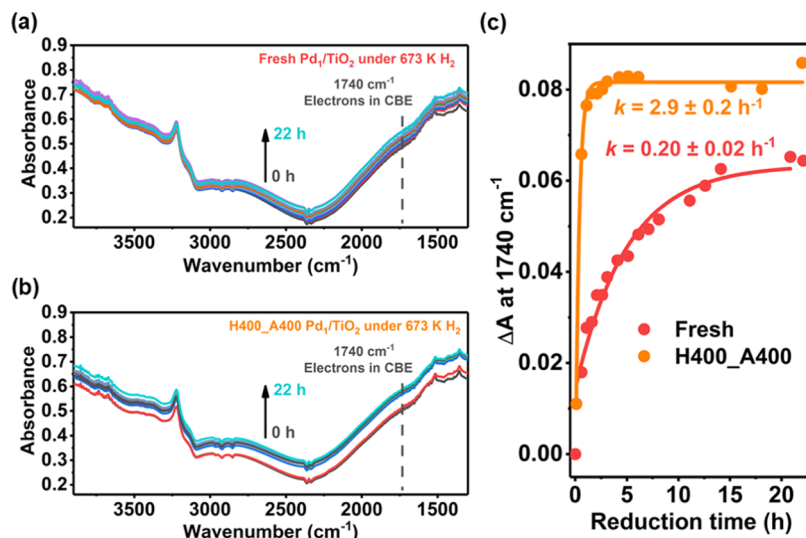


**Figure 8.** Evolution of IR spectra of 0.0125 wt % Pd<sub>1</sub>/TiO<sub>2</sub> under 1 Torr H<sub>2</sub> at 400 °C: (a, b) fresh and H400\_A400 (actual oxidation performed with 1 Torr O<sub>2</sub> in the vacuum chamber) samples, respectively. Spectra from the bottom (black) to the top (cyan) were collected at  $t = 0, 0.5, 1, 1.5, 2, 2.5, 3, 4, 5, 6, 8, 11, 12.5, 14, 20$ , and 22 h. (c) Variations in the relative absorbance ( $\Delta A$ ) at 1740 cm<sup>-1</sup> to  $t = 0$ , which reflects the amount of electrons injected into TiO<sub>2</sub>, with the reduction time. The data were fit exponentially and  $k$  is the pseudo-first-order rate constant for the TiO<sub>2</sub> reduction.

Pd<sub>1</sub>/TiO<sub>2</sub>: it has no Pd–Pd scattering and is best modeled by two Pd–O (directly bounded and next-next-neighbor) and one Pd–Ti paths (Figure S8a), with similar  $N(\text{Pd}–\text{O}_1)$  ( $4.0 \pm 0.5$  compared to  $3.2 \pm 0.4$ ). In XANES (Figure 7e), the white-line intensity, edge onset energy, and edge line shape of H400\_A400 Pd<sub>1</sub>/TiO<sub>2</sub> (orange) are all close to that of PdO (cyan) and fresh Pd<sub>1</sub>/TiO<sub>2</sub>. Therefore, all Pd on H400\_A400 Pd<sub>1</sub>/TiO<sub>2</sub> exist as Pd<sub>1</sub> in a similar coordination environment with Pd<sub>1</sub> on fresh Pd<sub>1</sub>/TiO<sub>2</sub>, i.e., Pd<sub>n</sub> can be redispersed into Pd<sub>1</sub> by high-temperature oxidation.

Surprisingly, H400\_A400 Pd<sub>1</sub>/TiO<sub>2</sub> shows a higher rWGS rate and faster rate increase with TOS (orange in Figure 7f) than fresh Pd<sub>1</sub>/TiO<sub>2</sub> (red), despite having spectroscopically similar Pd<sub>1</sub> sites with the latter. Directly oxidizing fresh Pd<sub>1</sub>/TiO<sub>2</sub> at 400 °C (“A400”) also has the promotion effects but treating it with 400 °C He does not (Figure S13), suggesting that the promotion is not due to pure thermal effects, such as TiO<sub>2</sub> dehydroxylation. After the activation by H<sub>2</sub>, the two samples also have Pd species of similar nuclearity and coordination environment (suggested by the highly similar EXAFS, “H400\_A400\_H400” and H400 in Figure S8b, Tables S2 and 1). Thus, the superior activity of H400\_A400 Pd<sub>1</sub>/TiO<sub>2</sub> cannot be attributed to the different Pd nuclearity or MSI structure. The difference between the two was revealed by IR: the triplet  $\nu(\text{CH})$  bands at 2963, 2928, and 2854 cm<sup>-1</sup> on fresh Pd<sub>1</sub>/TiO<sub>2</sub> disappear after 400 °C oxidation (Figure S14a). These bands are from mixed carboxylate layers adsorbed on TiO<sub>2</sub><sup>71–75</sup> from ppm-level carboxylic acids in air,<sup>76–78</sup> which is supported by XPS (Figure S14b). We have previously shown that the adsorbed carboxylate layers are detrimental to the rWGS catalysis,<sup>79</sup> and thus their removal explains the higher rWGS rate. This is supported by the results in Figure S13b: the promotion effect of the A400 treatment on Pd<sub>1</sub>/TiO<sub>2</sub> decays gradually with subsequent room-temperature air exposure during which the carboxylate layers would reaccumulate. We note that the A400 treatment also promotes the rWGS activity of pristine TiO<sub>2</sub>, which decays with room-temperature air exposure as well (Figure S15), further

supporting that the effects are due to changes on TiO<sub>2</sub>, and not of Pd.

Meanwhile, the rate increase with TOS is faster and more significant on H400\_A400 than over fresh Pd<sub>1</sub>/TiO<sub>2</sub>. Since the rate increase is due to changes in the Pd coordination environment caused by catalyst reduction, the observation infers that H400\_A400 Pd<sub>1</sub>/TiO<sub>2</sub> is easier to reduce than fresh Pd<sub>1</sub>/TiO<sub>2</sub>. For confirmation, we tracked the evolution of IR spectra of the two samples under H<sub>2</sub> at 400 °C, in which bulk TiO<sub>2</sub> reduction leads to increased absorbance between 2000 and 1200 cm<sup>-1</sup> as electrons are injected into the conduction band edge (CBE) of TiO<sub>2</sub>.<sup>80–82</sup> Figure 8a,b shows a series of IR spectra collected from the fresh and H400\_A400 Pd<sub>1</sub>/TiO<sub>2</sub>, respectively, and the changes in the IR absorbance ( $\Delta A$ ) in the CBE region (represented by 1740 cm<sup>-1</sup>) relative to  $t = 0$  h with the reduction time are shown in Figure 8c.  $\Delta A$  increases more than 10 times faster on H400\_A400 (orange in Figure 8c) than on fresh Pd<sub>1</sub>/TiO<sub>2</sub> (red), confirming the much more facile TiO<sub>2</sub> reduction on the former. This is likely due to the removal of the carboxylate layers reducing barriers for O<sub>v</sub>/electron migration. The faster, deeper bulk TiO<sub>2</sub> reduction (Figure 8c) coincides with the faster, more significant intrinsic activity increase of Pd (Figure 7f), and the time scale of the two processes aligns well (~22 h for bulk TiO<sub>2</sub> reduction, compared to ~25 h for the intrinsic activity increase), implying that the changes in Pd coordination environment under H<sub>2</sub> are likely driven by the bulk reduction of the anatase support.

**H<sub>2</sub>-Modified Pd Coordination Environment Mainly Promotes the Carboxyl rWGS Pathway.** We performed kinetic measurements on fresh and H400 Pd<sub>1</sub>/TiO<sub>2</sub> at various temperatures to reveal mechanistic origins of the high intrinsic activity of Pd in the coordination environment modified by H<sub>2</sub>. Figure 9a shows that both the rate enhancement (black) and the decrease in the apparent activation barrier ( $E_{a,\text{app}}$ , red and green for fresh and H400 Pd<sub>1</sub>/TiO<sub>2</sub>, respectively) after the activation by H<sub>2</sub> are more significant at a higher temperature (no rate enhancement, similar  $E_{a,\text{app}}$  at 200 °C; 3.6-fold rate increase, ~10 kJ/mol lower  $E_{a,\text{app}}$  at 350–400 °C). We have

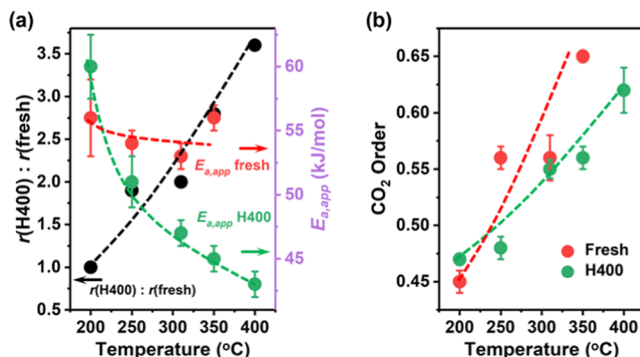


**Figure 9.** Measurements of the rWGS kinetics on fresh (red) and H400 (green)  $\text{Pd}_1/\text{TiO}_2$ : (a) variations in the rate enhancement level (black dots/curve), i.e., the rate ratio between the H400 and fresh samples, and the apparent activation barrier ( $E_{a,app}$ ) with the temperature and (b) variations in the reaction order with respect to  $\text{CO}_2$  with the temperature. Data cannot be obtained on fresh  $\text{Pd}_1/\text{TiO}_2$  at 400 °C due to the fast activation. The reactions were performed with a total flow of 40 SCCM,  $\text{H}_2$  concentration <25%,  $\text{CO}_2$  concentration <10%, and  $\text{CO}_2$  conversion <5%.

previously shown that on supported noble metal catalysts, the rWGS proceeds through both the formate (\* $\text{HCOO}$ ) pathway on large metal planes and the carboxyl (\* $\text{COOH}$ ) pathway on peripheral MSI sites.<sup>39,44,79,83–85</sup> Between the two, the carboxyl pathway contributes more at a higher temperature,<sup>39</sup> has lower  $E_{a,app}$  (~46 compared to ~64 kJ/mol,<sup>79</sup> Table S3), and higher reaction order with respect to  $\text{CO}_2$  (~0.61 compared to ~0.46,<sup>79</sup> Table S3). Figure 9b shows that as the reaction temperature increases from 200 to 400 °C, the  $\text{CO}_2$  order on both fresh and H400  $\text{Pd}_1/\text{TiO}_2$  increases from ~0.45 to ~0.63, reflecting the mechanism shift from the formate to the carboxyl pathway. Therefore, the more significant activation effects by  $\text{H}_2$  at a higher temperature in Figure 9a indicate that the modification of the Pd coordination environment mainly promotes the carboxyl pathway.

This conclusion matches the prediction from our previous mechanistic studies that the most active Pd sites for the carboxyl pathway are the ones at the MSI with a cleaved Pd–O interface with higher electron density than  $\text{Pd}(0)$ , created in situ by  $\text{H}_2$  reduction.<sup>39</sup> The elongated Pd–O bonds and unique electronic structure of Pd on H400  $\text{Pd}_1/\text{TiO}_2$  (in particular, the lower white-line intensity than metallic Pd) and the results obtained operando (Figure 4 and Table 1) align with the predicted active site structure, thus rationalizing the high intrinsic activity in the carboxyl pathway. The high

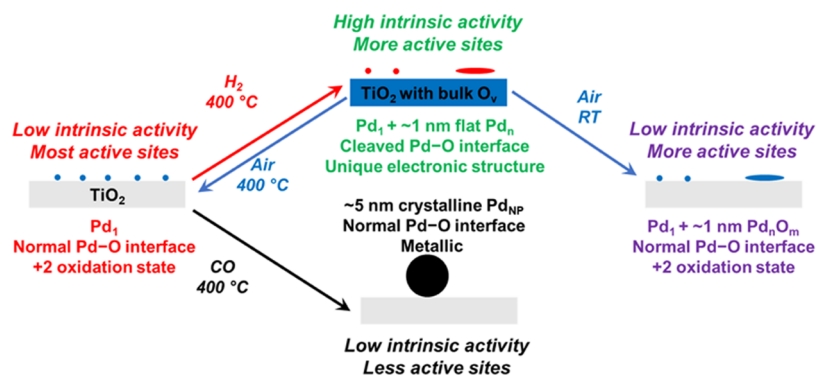
intrinsic activity of such Pd sites was attributed to their better ability to (1) activate  $\text{CO}_2$  and form the carboxyl intermediates, the rate-determining step of the carboxyl pathway<sup>39</sup> and (2) dissociate  $\text{H}_2$  as the back donation to the H–H antibonding orbital is stronger with higher electron density.<sup>17,86–88</sup>

## DISCUSSION

**Strong Effects of the Metal–Support Interaction on Highly Dispersed Metal Species.** We have demonstrated that the reduction of  $\text{TiO}_2$  by  $\text{H}_2$  partially cleaves its interface with supported  $\text{Pd}_1/\text{Pd}_{n\text{P}}$  modifies their electronic structure, which enhances their intrinsic activity in the rWGS. This occurs despite, not because of, the partial sintering of  $\text{Pd}_1$  to  $\text{Pd}_{n\text{P}}$ . The significant IR absorbance increase in the CBE region (Figure 8) and the blue color of H400  $\text{Pd}_1/\text{TiO}_2$  suggest a high reduction level of  $\text{TiO}_2$ . Nonetheless, no  $\text{Ti}^{3+}$  or  $\text{O}_v/\text{OH}$  were observed by the XPS (Figure S16a–c) in this catalyst, indicating that bulk  $\text{O}_v$  were formed rather than the surface  $\text{O}_v/-\text{OH}$ , in agreement with the literature for  $\text{TiO}_2\text{-A}$ .<sup>50–53</sup> Thus, the reduction of  $\text{TiO}_2\text{-A}$  alters the rWGS rate by changing the properties of Pd instead of the reactivity of its surfaces. This is supported by Figure S15, showing that reducing  $\text{TiO}_2\text{-A}$  alone does not enhance its rWGS activity and that the formation of the surface  $\text{Ce}^{3+}$  and  $\text{O}_v/\text{OH}$  on H400  $\text{Pd}/\text{CeO}_2$  (Figure S16d–f) does not increase the rWGS rate. The lack of  $\text{TiO}_2$  surface reduction on H400  $\text{Pd}/\text{TiO}_2\text{-A}$ , along with the lack of Pd–Ti scattering in the EXAFS (Figures 4a and S8b), also eliminates the possibility of the strong metal–support interaction (SMSI) causing the high activity. Since the coordination environment of single metal atoms is solely defined by the support, changes in support properties, even in the bulk, could affect their reactivity significantly. In contrast, CO400  $\text{Pd}_1/\text{TiO}_2$  exhibits minimal rate increase with TOS (Figure 2c), indicating that bulk  $\text{TiO}_2$  reduction has minimal effects on  $\text{Pd}_{n\text{P}}$ . This is because the coordination environment of Pd in  $\text{Pd}_{n\text{P}}$  is mostly determined by neighboring Pd, and thus less affected by the support. Also, on  $\text{Pd}_{n\text{P}}$ , a higher fraction of turnovers proceeds through the formate pathway that is not affected by the MSI.<sup>39</sup> We note that recent studies show that the effects of support reduction depend on its size<sup>89</sup> and that bulk  $\text{ZnO}$  reduction alters the electronic structure and reactivity of supported Au,<sup>90–93</sup> in concert with this work.

With all metal sites at the MSI, SACs carry unique values in mechanistic studies by enabling the direct observation of phenomena at the MSI that are difficult to probe on regular nanoparticle catalysts with ensemble-average characterization

**Scheme 1. Summary of the Structural Evolution of  $\text{Pd}_1/\text{TiO}_2$  SAC under Various Atmospheres**



techniques. The most active Pd sites for the carboxyl rWGS pathway, the electron-rich MSI sites with partially cleaved Pd–O bonds,  $\text{Pd}(\text{H})^\delta-\text{OH}$ , were previously predicted by theory<sup>39</sup> but not observed experimentally on nanoparticle catalysts. The XAS of H400\_Pd<sub>1</sub>/TiO<sub>2</sub> (Figure 4) provides experimental spectroscopic evidence for such sites. Although the minor sintering of Pd<sub>1</sub> reduces the fraction of MSI sites, the effect is alleviated by the flat shape of Pd<sub>n</sub>. The MSI cleavage under H<sub>2</sub> was previously reported on metal-oxide catalysts in a limited number of studies.<sup>61–67</sup> Similar to this work, these studies also used catalysts with highly dispersed metal species ( $d \leq 1 \text{ nm}$ ). We note that the  $\text{Pd}(\text{H})^\delta-\text{OH}$  active sites on Pd<sub>1</sub>/TiO<sub>2</sub> are only preserved under H<sub>2</sub> or during the rWGS and lost after being exposed to room-temperature air (Figure 7), or He (Figure S12). This emphasizes the necessity of *in situ*/operando spectroscopy in accurately understanding active sites on and dynamics of SACs.

**Dynamics of Pd<sub>1</sub>/TiO<sub>2</sub>-Anatase and Comparisons with Similar Systems.** The structural evolution of Pd<sub>1</sub> on TiO<sub>2</sub>-A is summarized in Scheme 1. The sintering of Pd<sub>1</sub> into ~5 nm crystalline Pd<sub>NP</sub> under 400 °C CO is expected considering the high mobility of Pd(CO)<sub>x</sub>, which aggregates even at room temperature.<sup>35</sup> In contrast, under H<sub>2</sub>, only some Pd<sub>1</sub> sinter into ~1 nm disordered Pd<sub>n</sub>. The contrast of Pd<sub>n</sub> with TiO<sub>2</sub> in STEM images ranges from two-dimensional (2D)-like to similar with regular particles, suggesting various thicknesses. In the EXAFS, completely 2D fcc metal clusters have no M–M<sub>2</sub> scattering ( $R = 3.83 \text{ \AA}$  for Pd).<sup>94–96</sup> Thus, the lower  $N(\text{Pd}-\text{Pd}_2)$  of Pd<sub>n</sub> than the expectation from hemispherical shape reflects the on-average flattened shape. We note that the total  $N(\text{Pd}-\text{O}) = 3.1 \pm 0.3$  on H400\_Pd<sub>1</sub>/TiO<sub>2</sub> is high for Pd clusters of  $d \approx 1.2 \text{ nm}$ . This is due to both the presence of some Pd<sub>1</sub> (Figure 3b) and the fact that flattened plates have more Pd in contact with the support oxygen than same-sized hemispherical particles.<sup>94</sup> The flattened, disordered, small M<sub>n</sub> were reported to form under H<sub>2</sub> from other M<sub>1</sub> on reducible oxides as well<sup>37,96</sup> and proposed to be stabilized by the electron transfer from the reduced support.<sup>37,97–101</sup> This hypothesis is supported by the fact that H400\_A400\_H400\_Pd<sub>1</sub>/TiO<sub>2</sub>, which has more reduced TiO<sub>2</sub> (Figure 8c) than H400\_Pd<sub>1</sub>/TiO<sub>2</sub>, have completely flat Pd<sub>n</sub>, as suggested by  $N(\text{Pd}-\text{Pd}_2) = 0$  (Table S2). Thus, when TiO<sub>2</sub> is oxidized by air, Pd<sub>n</sub> become unstable. At room temperature, the barrier for the redispersion cannot be overcome, but Pd<sub>n</sub> are oxidized (Figure 7 and Table S2) to Pd<sub>n</sub><sup>2+</sup>O<sub>m</sub>, while under the same conditions, crystalline, three-dimensional Pd<sub>NP</sub> mostly remain metallic (Figure 4 and Table 1). At 400 °C, they are completely redispersed into Pd<sub>1</sub> (Figure 7).

During the rWGS, the coexistence of H<sub>2</sub> and CO leads to a mixture of Pd<sub>1</sub>, Pd<sub>n</sub> and Pd<sub>NP</sub>, as shown by STEM images of the post-reaction sample (Figure S17). This is further supported by the observation that all XAS characteristics of Pd<sub>1</sub>/TiO<sub>2</sub> used in the rWGS after room-temperature air exposure (“RWGS400\_ART”) are between those of H400\_ART and CO400\_ART Pd<sub>1</sub>/TiO<sub>2</sub> (Figure S18 and Table S2). When the conversion and thus CO concentration is low, its effects on both rates (Figure 2b) and Pd structure (Figure 4) become negligible. At low Pd<sub>1</sub> coverage ( $\leq 0.025 \text{ wt \%}$ ), sintering is minor. Thus, the higher intrinsic activity due to the activation by H<sub>2</sub> overcomes the decrease in dispersion, and the per-Pd reaction rate increases (Figure 1a). At high Pd<sub>1</sub> coverage (0.05 wt %), the two effects offset, leading to minimal rate changes with TOS. Since sintering is less demanding and

faster than the activation by H<sub>2</sub>, at  $\leq 375 \text{ }^\circ\text{C}$ , the rate drop due to sintering can be captured initially (Figure 1b). Accounting for the sintering and assuming MSI active sites,<sup>39,44</sup> the 3.6-fold rate increase after the activation by H<sub>2</sub> corresponds with a ~4.5-fold increase in TOF.

The activation by H<sub>2</sub> of Pd<sub>1</sub>/TiO<sub>2</sub> demands  $T \geq 350 \text{ }^\circ\text{C}$  (Figure 1b) and has a high activation barrier of ~120 kJ/mol (Figure S4), suggesting that it cannot be explained simply by Pd–H binding. This high barrier could be associated with O<sub>v</sub> migration into anatase bulk (70–80 kJ/mol in the literature).<sup>51,52,102</sup> In addition, as DFT suggests (Figure 6), Pd likely diffuses to other surface sites under H<sub>2</sub>, which may also have high barriers (~100 kJ/mol in the literature for Pt<sub>1</sub> diffusion on anatase<sup>103,104</sup>). The process can be facilitated by higher H<sub>2</sub> pressure, as under high-pressure rWGS conditions (Figure S19, 21 bar H<sub>2</sub>), the intrinsic activity increase can be observed at 300 °C and on Pd<sub>NP</sub>.

Finally, we compare the dynamics of Pd<sub>1</sub>/TiO<sub>2</sub> with systems we previously studied.<sup>27,37</sup> On TiO<sub>2</sub>-A at 400 °C, Pt<sub>1</sub> also form stable, crystalline Pt<sub>NP</sub> under CO, and ~1 nm, disordered, flat Pt<sub>n</sub> under H<sub>2</sub>. Nonetheless, the Pt–O interface remains intact under H<sub>2</sub>, and thus the reduction does not increase the rWGS rate.<sup>37</sup> The contrast between Pt and Pd again emphasizes that the rWGS activity of highly dispersed Pd/Pt is determined by their coordination environment, rather than nuclearity. The flat shape and small size (~1 nm) of Pt<sub>n</sub>/Pd<sub>n</sub> predict that ~80% Pt/Pd sites are at MSI, explaining the similar rWGS rate between fresh and H400\_ART Pd<sub>1</sub>/TiO<sub>2</sub> (Figure 7f). Pt and Pd also behave differently in the oxidative redispersion, which occurs at room temperature for Pt<sup>37</sup> but requires a high temperature for Pd. Furthermore, the redispersed Pt<sub>1</sub> is in a different environment from the fresh Pt<sub>1</sub>,<sup>37</sup> while fresh and redispersed Pd<sub>1</sub> are spectroscopically similar. On the other hand, TiO<sub>2</sub>-R traps Pd<sub>1</sub> in the surface O<sub>v</sub> when reduced at 400 °C,<sup>27</sup> while TiO<sub>2</sub>-A does not because the surface O<sub>v</sub> is not thermodynamically favored on anatase.<sup>49–52</sup> The comparisons, along with the fact that the intrinsic activity increase is unique to Pd/TiO<sub>2</sub>-A among all metal–support combinations (Figure 1c,d), emphasize that the dynamics of SACs are highly dependent on the properties of the metal and support, and are thus difficult to generalize. The physical origin of the different behaviors of other metal–support pairs could be a topic of future studies.

## CONCLUSIONS

This paper discusses the dynamic changes in the coordination environment and nuclearity of Pd<sub>1</sub> on anatase TiO<sub>2</sub> under conditions related to the rWGS, and their catalytic consequences. At  $T \geq 350 \text{ }^\circ\text{C}$ , the rWGS rate increases with TOS, which is unique to Pd<sub>1</sub> on TiO<sub>2</sub>-A. The activation is driven by H<sub>2</sub> in the reaction stream, while the CO product deactivates the catalyst. *In situ*/operando XAS revealed that the bulk reduction of TiO<sub>2</sub> by H<sub>2</sub> or the reaction stream partially cleaves the Pd–O interface and modifies the electronic structure of Pd. The new coordination environment of Pd sites facilitates rWGS turnover through the carboxyl pathway, which overcomes the minor sintering of some Pd<sub>1</sub> into disordered, flattened Pd<sub>n</sub> of  $d \approx 1 \text{ nm}$ . Such changes in the Pd coordination environment are reversed under air, which at 400 °C, also redisperses Pd<sub>n</sub> into Pd<sub>1</sub> and promotes both the rWGS turnover and TiO<sub>2</sub> reduction by removing the auto-adsorbed carboxylate layers on TiO<sub>2</sub>. On the other hand, the deactivation by CO is due to Pd<sub>1</sub> sintering into crystalline Pd<sub>NP</sub>.

of  $d \approx 5$  nm. This work elucidates the complicated dynamics of Pd<sub>1</sub>/TiO<sub>2</sub> under pretreatment and operando conditions, enhancing the fundamental understanding of SACs. It reveals the unique metal coordination environment leading to high intrinsic rWGS activity, establishing the instructive but often elusive structure–function relationship on SACs.

## ■ ASSOCIATED CONTENT

### § Supporting Information

The Supporting Information is available free of charge at <https://pubs.acs.org/doi/10.1021/jacs.3c02326>.

Experimental methods; supporting characterization data and related analysis (IR, XAS, XPS, TEM); supporting rWGS kinetic data; kinetic modeling of Pd evolution under H<sub>2</sub>; supporting structural information from the simulation (DFT and MD); and typical kinetic parameters for the two rWGS reaction pathways ([PDF](#))

## ■ AUTHOR INFORMATION

### Corresponding Author

János Szanyi – Pacific Northwest National Laboratory, Richland, Washington 99352, United States;  [orcid.org/0000-0002-8442-5465](#); Email: [janos.szanyi@pnnl.gov](mailto:janos.szanyi@pnnl.gov)

### Authors

Linxiao Chen – Pacific Northwest National Laboratory, Richland, Washington 99352, United States

Sarah I. Allec – Pacific Northwest National Laboratory, Richland, Washington 99352, United States;  [orcid.org/0000-0002-1101-3160](#)

Manh-Thuong Nguyen – Pacific Northwest National Laboratory, Richland, Washington 99352, United States;  [orcid.org/0000-0003-1997-0368](#)

Libor Kovarik – Pacific Northwest National Laboratory, Richland, Washington 99352, United States

Adam S. Hoffman – Stanford Synchrotron Radiation Lightsource, SLAC National Accelerator Laboratory, Menlo Park, California 94025, United States;  [orcid.org/0000-0002-7682-4108](#)

Jiyun Hong – Stanford Synchrotron Radiation Lightsource, SLAC National Accelerator Laboratory, Menlo Park, California 94025, United States

Debora Meira – Canadian Light Source Inc., Saskatoon, Saskatchewan S7N 2V3, Canada

Honghong Shi – Pacific Northwest National Laboratory, Richland, Washington 99352, United States

Simon R. Bare – Stanford Synchrotron Radiation Lightsource, SLAC National Accelerator Laboratory, Menlo Park, California 94025, United States

Vassiliki-Alexandra Glezakou – Pacific Northwest National Laboratory, Richland, Washington 99352, United States;  [orcid.org/0000-0001-6028-7021](#)

Roger Rousseau – Pacific Northwest National Laboratory, Richland, Washington 99352, United States; Present Address: Oak Ridge National Laboratory, Oak Ridge, TN 37830, United States;  [orcid.org/0000-0003-1947-0478](#)

Complete contact information is available at:

<https://pubs.acs.org/10.1021/jacs.3c02326>

### Notes

The authors declare no competing financial interest.

## ■ ACKNOWLEDGMENTS

This work was supported by the U.S. Department of Energy, Office of Science, Basic Energy Sciences, Chemical Sciences, Geosciences, and Biosciences Division, Catalysis Science Program, FWP 47319. PNNL is a multiprogram National Laboratory operated for DOE by Battelle. The authors acknowledge Dr. Mark E. Bowden, X. Shari Li, Mark Engelhard, and Dr. Yiqing Wu at PNNL for XRD, BET, and XPS measurements, and material synthesis. Use of the Stanford Synchrotron Radiation Lightsource, SLAC National Accelerator Laboratory, is supported by the U.S. Department of Energy, Office of Science, Office of Basic Energy Sciences under Contract No. DE-AC02-76SF00515. This research used resources of the National Energy Research Scientific Computing Center, a DOE Office of Science User Facility supported by the Office of Science of the U.S. Department of Energy under Contract No. DE-AC02-05CH11231. Co-ACCESS is supported by the U.S. Department of Energy, Office of Basic Energy Sciences, Chemical Sciences, Geosciences and Bioscience Division. This research used resources of the Advanced Photon Source (APS), an Office of Science User Facility operated for the U.S. Department of Energy (DOE) Office of Science by Argonne National Laboratory and was supported by the U.S. DOE under Contract No. DE-AC02-06CH11357 and the Canadian Light Source and its funding partners.

## ■ REFERENCES

- (1) Li, Z.; Ji, S.; Liu, Y.; Cao, X.; Tian, S.; Chen, Y.; Niu, Z.; Li, Y. Well-Defined Materials for Heterogeneous Catalysis: From Nanoparticles to Isolated Single-Atom Sites. *Chem. Rev.* **2020**, *120*, 623–682.
- (2) Cui, X.; Li, W.; Ryabchuk, P.; Junge, K.; Beller, M. Bridging homogeneous and heterogeneous catalysis by heterogeneous single-metal-site catalysts. *Nat. Catal.* **2018**, *1*, 385–397.
- (3) Chen, Y.; Huang, Z.; Ma, Z.; Chen, J.; Tang, X. Fabrication, characterization, and stability of supported single-atom catalysts. *Catal. Sci. Technol.* **2017**, *7*, 4250–4258.
- (4) Liu, P.; Zhao, Y.; Qin, R.; Mo, S.; Chen, G.; Gu, L.; Chevrier, D. M.; Zhang, P.; Guo, Q.; Zang, D.; et al. Photochemical route for synthesizing atomically dispersed palladium catalysts. *Science* **2016**, *352*, 797–800.
- (5) Jones, J.; Xiong, H.; DeLaRiva, A. T.; Peterson, E. J.; Pham, H.; Challa, S. R.; Qi, G.; Oh, S.; Wiebenga, M. H.; Hernández, X. I. P.; et al. Thermally stable single-atom platinum-on-ceria catalysts via atom trapping. *Science* **2016**, *353*, 150–154.
- (6) Piernavieja-Hermida, M.; Lu, Z.; White, A.; Low, K.-B.; Wu, T.; Elam, J. W.; Wu, Z.; Lei, Y. Towards ALD thin film stabilized single-atom Pd1 catalysts. *Nanoscale* **2016**, *8*, 15348–15356.
- (7) Jiao, L.; Regalbuto, J. R. The synthesis of highly dispersed noble and base metals on silica via strong electrostatic adsorption: I. Amorphous silica. *J. Catal.* **2008**, *260*, 329–341.
- (8) Chen, L.; Sterbinsky, G. E.; Tait, S. L. Synthesis of platinum single-site centers through metal-ligand self-assembly on powdered metal oxide supports. *J. Catal.* **2018**, *365*, 303–312.
- (9) Li, X.; Yang, X.; Zhang, J.; Huang, Y.; Liu, B. In Situ/Operando Techniques for Characterization of Single-Atom Catalysts. *ACS Catal.* **2019**, *9*, 2521–2531.
- (10) Li, Y.; Frenkel, A. I. Deciphering the Local Environment of Single-Atom Catalysts with X-ray Absorption Spectroscopy. *Acc. Chem. Res.* **2021**, *54*, 2660–2669.
- (11) Asokan, C.; DeRita, L.; Christopher, P. Using probe molecule FTIR spectroscopy to identify and characterize Pt-group metal based single atom catalysts. *Chin. J. Catal.* **2017**, *38*, 1473–1480.
- (12) Kyriakou, G.; Boucher, M. B.; Jewell, A. D.; Lewis, E. A.; Lawton, T. J.; Baber, A. E.; Tierney, H. L.; Flytzani-Stephanopoulos,

- M.; Sykes, E. C. H. Isolated Metal Atom Geometries as a Strategy for Selective Heterogeneous Hydrogenations. *Science* **2012**, *335*, 1209–1212.
- (13) DeRita, L.; Dai, S.; Lopez-Zepeda, K.; Pham, N.; Graham, G. W.; Pan, X.; Christopher, P. Catalyst Architecture for Stable Single Atom Dispersion Enables Site-Specific Spectroscopic and Reactivity Measurements of CO Adsorbed to Pt Atoms, Oxidized Pt Clusters, and Metallic Pt Clusters on TiO<sub>2</sub>. *J. Am. Chem. Soc.* **2017**, *139*, 14150–14165.
- (14) Chen, L.; Ali, I. S.; Sterbinsky, G. E.; Gamler, J. T. L.; Skrabalak, S. E.; Tait, S. L. Alkene Hydrosilylation on Oxide-Supported Pt-Ligand Single-Site Catalysts. *ChemCatChem* **2019**, *11*, 2843–2854.
- (15) Chen, Z.; Vorobyeva, E.; Mitchell, S.; Fako, E.; Ortúñoz, M. A.; López, N.; Collins, S. M.; Midgley, P. A.; Richard, S.; Vilé, G.; Pérez-Ramírez, J. A heterogeneous single-atom palladium catalyst surpassing homogeneous systems for Suzuki coupling. *Nat. Nanotechnol.* **2018**, *13*, 702–707.
- (16) Macino, M.; Barnes, A. J.; Althahban, S. M.; Qu, R.; Gibson, E. K.; Morgan, D. J.; Freakley, S. J.; Dimitratos, N.; Kiely, C. J.; Gao, X.; et al. Tuning of catalytic sites in Pt/TiO<sub>2</sub> catalysts for the chemoselective hydrogenation of 3-nitrostyrene. *Nat. Catal.* **2019**, *2*, 873–881.
- (17) Chen, L.; Ali, I. S.; Sterbinsky, G. E.; Zhou, X.; Wasim, E.; Tait, S. L. Ligand-coordinated Ir single-atom catalysts stabilized on oxide supports for ethylene hydrogenation and their evolution under a reductive atmosphere. *Catal. Sci. Technol.* **2021**, *11*, 2081–2093.
- (18) Malta, G.; Freakley, S. J.; Kondrat, S. A.; Hutchings, G. J. Acetylene hydrochlorination using Au/carbon: a journey towards single site catalysis. *Chem. Commun.* **2017**, *53*, 11733–11746.
- (19) Yang, M.; Liu, J.; Lee, S.; Zugic, B.; Huang, J.; Allard, L. F.; Flytzani-Stephanopoulos, M. A Common Single-Site Pt(II)–O(OH)<sub>x</sub>– Species Stabilized by Sodium on “Active” and “Inert” Supports Catalyzes the Water-Gas Shift Reaction. *J. Am. Chem. Soc.* **2015**, *137*, 3470–3473.
- (20) Ding, K.; Gulec, A.; Johnson, A. M.; Schweitzer, N. M.; Stucky, G. D.; Marks, L. D.; Stair, P. C. Identification of active sites in CO oxidation and water-gas shift over supported Pt catalysts. *Science* **2015**, *350*, 189–192.
- (21) Wang, Y.-G.; Mei, D.; Glezaou, V.-A.; Li, J.; Rousseau, R. Dynamic formation of single-atom catalytic active sites on ceria-supported gold nanoparticles. *Nat. Commun.* **2015**, *6*, No. 6511.
- (22) Huang, F.; Deng, Y.; Chen, Y.; Cai, X.; Peng, M.; Jia, Z.; Ren, P.; Xiao, D.; Wen, X.; Wang, N.; et al. Atomically Dispersed Pd on Nanodiamond/Graphene Hybrid for Selective Hydrogenation of Acetylene. *J. Am. Chem. Soc.* **2018**, *140*, 13142–13146.
- (23) Tang, Y.; Asokan, C.; Xu, M.; Graham, G. W.; Pan, X.; Christopher, P.; Li, J.; Sautet, P. Rh single atoms on TiO<sub>2</sub> dynamically respond to reaction conditions by adapting their site. *Nat. Commun.* **2019**, *10*, No. 4488.
- (24) Daelman, N.; Capdevila-Cortada, M.; López, N. Dynamic charge and oxidation state of Pt/CeO<sub>2</sub> single-atom catalysts. *Nat. Mater.* **2019**, *18*, 1215–1221.
- (25) Li, H.; Wang, M.; Luo, L.; Zeng, J. Static Regulation and Dynamic Evolution of Single-Atom Catalysts in Thermal Catalytic Reactions. *Adv. Sci.* **2019**, *6*, No. 1801471.
- (26) Hu, P.; Huang, Z.; Amghous, Z.; Makkee, M.; Xu, F.; Kapteijn, F.; Dikhtierenko, A.; Chen, Y.; Gu, X.; Tang, X. Electronic Metal-Support Interactions in Single-Atom Catalysts. *Angew. Chem., Int. Ed.* **2014**, *53*, 3418–3421.
- (27) Nelson, N. C.; Chen, L.; Meira, D.; Kovarik, L.; Szanyi, J. In Situ Dispersion of Palladium on TiO<sub>2</sub> During Reverse Water–Gas Shift Reaction: Formation of Atomically Dispersed Palladium. *Angew. Chem., Int. Ed.* **2020**, *59*, 17657–17663.
- (28) DeRita, L.; Resasco, J.; Dai, S.; Boubnov, A.; Thang, H. V.; Hoffman, A. S.; Ro, I.; Graham, G. W.; Bare, S. R.; Pacchioni, G.; et al. Structural evolution of atomically dispersed Pt catalysts dictates reactivity. *Nat. Mater.* **2019**, *18*, 746–751.
- (29) Muravev, V.; Spezzati, G.; Su, Y.-Q.; Parastaev, A.; Chiang, F.-K.; Longo, A.; Escudero, C.; Kosinov, N.; Hensen, E. J. M. Interface dynamics of Pd–CeO<sub>2</sub> single-atom catalysts during CO oxidation. *Nat. Catal.* **2021**, *4*, 469–478.
- (30) Gates, B. C.; Flytzani-Stephanopoulos, M.; Dixon, D. A.; Katz, A. Atomically dispersed supported metal catalysts: perspectives and suggestions for future research. *Catal. Sci. Technol.* **2017**, *7*, 4259–4275.
- (31) Hoffman, A. S.; Debefve, L. M.; Zhang, S.; Perez-Aguilar, J. E.; Conley, E. T.; Justl, K. R.; Arslan, I.; Dixon, D. A.; Gates, B. C. Beating Heterogeneity of Single-Site Catalysts: MgO-Supported Iridium Complexes. *ACS Catal.* **2018**, *8*, 3489–3498.
- (32) Hoffman, A. S.; Fang, C.-Y.; Gates, B. C. Homogeneity of Surface Sites in Supported Single-Site Metal Catalysts: Assessment with Band Widths of Metal Carbonyl Infrared Spectra. *J. Phys. Chem. Lett.* **2016**, *7*, 3854–3860.
- (33) Doudin, N.; Yuk, S. F.; Marcinkowski, M. D.; Nguyen, M.-T.; Liu, J.-C.; Wang, Y.; Novotny, Z.; Kay, B. D.; Li, J.; Glezaou, V.-A.; et al. Understanding Heterolytic H<sub>2</sub> Cleavage and Water-Assisted Hydrogen Spillover on Fe<sub>3</sub>O<sub>4</sub>(001)-Supported Single Palladium Atoms. *ACS Catal.* **2019**, *9*, 7876–7887.
- (34) Bliem, R.; van der Hoeven, J.; Zavodny, A.; Gamba, O.; Pavleček, J.; de Jongh, P. E.; Schmid, M.; Diebold, U.; Parkinson, G. S. An Atomic-Scale View of CO and H<sub>2</sub> Oxidation on a Pt/Fe<sub>3</sub>O<sub>4</sub> Model Catalyst. *Angew. Chem., Int. Ed.* **2015**, *54*, 13999–14002.
- (35) Parkinson, G. S.; Novotny, Z.; Argentero, G.; Schmid, M.; Pavleček, J.; Kosak, R.; Blaha, P.; Diebold, U. Carbon monoxide-induced adatom sintering in a Pd–Fe<sub>3</sub>O<sub>4</sub> model catalyst. *Nat. Mater.* **2013**, *12*, 724–728.
- (36) Wang, H.; Liu, J.-X.; Allard, L. F.; Lee, S.; Liu, J.; Li, H.; Wang, J.; Wang, J.; Oh, S. H.; Li, W.; et al. Surpassing the single-atom catalytic activity limit through paired Pt–O–Pt ensemble built from isolated PtI atoms. *Nat. Commun.* **2019**, *10*, No. 3808.
- (37) Chen, L.; Unocic, R. R.; Hoffman, A. S.; Hong, J.; Braga, A. H.; Bao, Z.; Bare, S. R.; Szanyi, J. Unlocking the Catalytic Potential of TiO<sub>2</sub>-Supported Pt Single Atoms for the Reverse Water–Gas Shift Reaction by Altering Their Chemical Environment. *JACS Au* **2021**, *1*, 977–986.
- (38) Asokan, C.; Thang, H. V.; Pacchioni, G.; Christopher, P. Reductant composition influences the coordination of atomically dispersed Rh on anatase TiO<sub>2</sub>. *Catal. Sci. Technol.* **2020**, *10*, 1597–1601.
- (39) Nelson, N. C.; Nguyen, M.-T.; Glezaou, V.-A.; Rousseau, R.; Szanyi, J. Carboxyl intermediate formation via an in situ-generated metastable active site during water-gas shift catalysis. *Nat. Catal.* **2019**, *2*, 916–924.
- (40) Wu, H. C.; Chang, Y. C.; Wu, J. H.; Lin, J. H.; Lin, I. K.; Chen, C. S. Methanation of CO<sub>2</sub> and reverse water gas shift reactions on Ni/SiO<sub>2</sub> catalysts: the influence of particle size on selectivity and reaction pathway. *Catal. Sci. Technol.* **2015**, *5*, 4154–4163.
- (41) Wang, L. C.; Khazaneh, M. T.; Widmann, D.; Behm, R. J. TAP reactor studies of the oxidizing capability of CO<sub>2</sub> on a Au/CeO<sub>2</sub> catalyst – A first step toward identifying a redox mechanism in the Reverse Water–Gas Shift reaction. *J. Catal.* **2013**, *302*, 20–30.
- (42) Rodriguez, J. A.; Evans, J.; Feria, L.; Vidal, A. B.; Liu, P.; Nakamura, K.; Illas, F. CO<sub>2</sub> hydrogenation on Au/TiC, Cu/TiC, and Ni/TiC catalysts: Production of CO, methanol, and methane. *J. Catal.* **2013**, *307*, 162–169.
- (43) Erdőhelyi, A.; Pásztor, M.; Solymosi, F. Catalytic hydrogenation of CO<sub>2</sub> over supported palladium. *J. Catal.* **1986**, *98*, 166–177.
- (44) Nelson, N. C.; Szanyi, J. Heterolytic Hydrogen Activation: Understanding Support Effects in Water–Gas Shift, Hydrodeoxyge nation, and CO Oxidation Catalysis. *ACS Catal.* **2020**, *10*, 5663–5671.
- (45) Kwak, J. H.; Kovarik, L.; Szanyi, J. Heterogeneous Catalysis on Atomically Dispersed Supported Metals: CO<sub>2</sub> Reduction on Multi-functional Pd Catalysts. *ACS Catal.* **2013**, *3*, 2094–2100.

- (46) Kwak, J. H.; Kovarik, L.; Szanyi, J. CO<sub>2</sub> Reduction on Supported Ru/Al<sub>2</sub>O<sub>3</sub> Catalysts: Cluster Size Dependence of Product Selectivity. *ACS Catal.* **2013**, *3*, 2449–2455.
- (47) Matsubu, J. C.; Yang, V. N.; Christopher, P. Isolated Metal Active Site Concentration and Stability Control Catalytic CO<sub>2</sub> Reduction Selectivity. *J. Am. Chem. Soc.* **2015**, *137*, 3076–3084.
- (48) Patra, S.; Davoisne, C.; Bouyanfif, H.; Foix, D.; Sauvage, F. Phase stability frustration on ultra-nanosized anatase TiO<sub>2</sub>. *Sci. Rep.* **2015**, *5*, No. 10928.
- (49) Di Valentin, C.; Pacchioni, G.; Selloni, A. Reduced and n-Type Doped TiO<sub>2</sub>: Nature of Ti<sup>3+</sup> Species. *J. Phys. Chem. C* **2009**, *113*, 20543–20552.
- (50) Cheng, H.; Selloni, A. Surface and subsurface oxygen vacancies in anatase TiO<sub>2</sub> and differences with rutile. *Phys. Rev. B* **2009**, *79*, No. 092101.
- (51) Cheng, H.; Selloni, A. Energetics and diffusion of intrinsic surface and subsurface defects on anatase TiO<sub>2</sub>(101). *J. Chem. Phys.* **2009**, *131*, No. 054703.
- (52) Islam, M. M.; Calatayud, M.; Pacchioni, G. Hydrogen Adsorption and Diffusion on the Anatase TiO<sub>2</sub>(101) Surface: A First-Principles Investigation. *J. Phys. Chem. C* **2011**, *115*, 6809–6814.
- (53) Diebold, U. The surface science of titanium dioxide. *Surf. Sci. Rep.* **2003**, *48*, 53–229.
- (54) Zhang, H.; Banfield, J. F. Thermodynamic analysis of phase stability of nanocrystalline titania. *J. Mater. Chem.* **1998**, *8*, 2073–2076.
- (55) Hadjiivanov, K. I.; Klissurski, D. G. Surface chemistry of titania (anatase) and titania-supported catalysts. *Chem. Soc. Rev.* **1996**, *25*, 61–69.
- (56) Wolter, K.; Seiferth, O.; Libuda, J.; Kuhlenbeck, H.; Bäumer, M.; Freund, H.-J. Infrared study of CO adsorption on alumina supported palladium particles. *Surf. Sci.* **1998**, *402*–404, 428–432.
- (57) Bensalem, A.; Muller, J.-C.; Tessier, D.; Bozon-Verduraz, F. Spectroscopic study of CO adsorption on palladium–ceria catalysts. *J. Chem. Soc., Faraday Trans.* **1996**, *92*, 3233–3237.
- (58) Tessier, D.; Rakai, A.; Bozon-Verduraz, F. Spectroscopic study of the interaction of carbon monoxide with cationic and metallic palladium in palladium–alumina catalysts. *J. Chem. Soc., Faraday Trans.* **1992**, *88*, 741–749.
- (59) Vannice, M. A.; Wang, S. Y. Determination of IR extinction coefficients for linear- and bridged-bonded carbon monoxide on supported palladium. *J. Phys. Chem. A* **1981**, *85*, 2543–2546.
- (60) Jentys, A. Estimation of mean size and shape of small metal particles by EXAFS. *Phys. Chem. Chem. Phys.* **1999**, *1*, 4059–4063.
- (61) Vaarkamp, M.; Modica, F. S.; Miller, J. T.; Koningsberger, D. C. Influence of Hydrogen Pretreatment on the Structure of the Metal-Support Interface in Pt/Zeolite Catalysts. *J. Catal.* **1993**, *144*, 611–626.
- (62) Koningsberger, D. C.; Gates, B. C. Nature of the metal-support interface in supported metal catalysts: Results from X-ray absorption spectroscopy. *Catal. Lett.* **1992**, *14*, 271–277.
- (63) Moller, K.; Koningsberger, D. C.; Bein, T. Stabilization of metal ensembles at room temperature: palladium clusters in zeolites. *J. Phys. Chem. B* **1989**, *93*, 6116–6120.
- (64) Martens, J. H. A.; Prins, R.; Zandbergen, H.; Koningsberger, D. C. Structure of rhodium/titania in the normal and the SMSI state as determined by extended x-ray absorption fine structure and high-resolution transmission electron microscopy. *J. Phys. Chem. C* **1988**, *92*, 1903–1916.
- (65) Koningsberger, D. C.; Sayers, D. E. An EXAFS study of platinum - oxygen bonds in the metal-support interface of a highly dispersed Pt/Al<sub>2</sub>O<sub>3</sub> catalyst. *Solid State Ionics* **1985**, *16*, 23–27.
- (66) Van't Blik, H. F. J.; Van Zon, J. B. A. D.; Huizinga, T.; Vis, J. C.; Koningsberger, D. C.; Prins, R. Structure of rhodium in an ultradispersed rhodium/alumina catalyst as studied by EXAFS and other techniques. *J. Am. Chem. Soc.* **1985**, *107*, 3139–3147.
- (67) Koningsberger, D. C.; Van Zon, J. B. A. D.; Van't Blik, H. F. J.; Visser, G. J.; Prins, R.; Mansour, A. N.; Sayers, D. E.; Short, D. R.; Katzer, J. R. An extended x-ray absorption fine structure study of rhodium-oxygen bonds in a highly dispersed rhodium/aluminum oxide catalyst. *J. Phys. Chem. D* **1985**, *89*, 4075–4081.
- (68) Bond, G. C.; Coq, B.; Dutartre, R.; Ruiz, J. G.; Hooper, A. D.; Proietti, M. G.; Sierra, M. C. S.; Slaa, J. C. Effect of Various Pretreatments on the Structure and Properties of Ruthenium Catalysts. *J. Catal.* **1996**, *161*, 480–494.
- (69) Zaki, M. I.; Kunzmann, G.; Gates, B. C.; Knoeziinger, H. Highly dispersed rhodium on alumina catalysts: influence of the atmosphere on the state and dispersion of rhodium. *J. Phys. Chem. E* **1987**, *91*, 1486–1493.
- (70) Jin, C.; Dai, Y.; Wei, W.; Ma, X.; Li, M.; Huang, B. Effects of single metal atom (Pt, Pd, Rh and Ru) adsorption on the photocatalytic properties of anatase TiO<sub>2</sub>. *Appl. Surf. Sci.* **2017**, *426*, 639–646.
- (71) Hasan, M. A.; Zaki, M. I.; Pasupulety, L. Oxide-catalyzed conversion of acetic acid into acetone: an FTIR spectroscopic investigation. *Appl. Catal., A* **2003**, *243*, 81–92.
- (72) Pei, Z. F.; Ponec, V. On the intermediates of the acetic acid reactions on oxides: an IR study. *Appl. Surf. Sci.* **1996**, *103*, 171–182.
- (73) Mattsson, A.; Österlund, L. Adsorption and Photoinduced Decomposition of Acetone and Acetic Acid on Anatase, Brookite, and Rutile TiO<sub>2</sub> Nanoparticles. *J. Phys. Chem. C* **2010**, *114*, 14121–14132.
- (74) Sun, Z.; Kong, L.; Ding, X.; Du, C.; Zhao, X.; Chen, J.; Fu, H.; Yang, X.; Cheng, T. The effects of acetaldehyde, glyoxal and acetic acid on the heterogeneous reaction of nitrogen dioxide on gamma-alumina. *Phys. Chem. Chem. Phys.* **2016**, *18*, 9367–9376.
- (75) Backes, M. J.; Lukaski, A. C.; Muggli, D. S. Active sites and effects of H<sub>2</sub>O and temperature on the photocatalytic oxidation of 13C-acetic acid on TiO<sub>2</sub>. *Appl. Catal., B* **2005**, *61*, 21–35.
- (76) Balajka, J.; Hines, M. A.; DeBenedetti, W. J. I.; Komara, M.; Pavleček, J.; Schmid, M.; Diebold, U. High-affinity adsorption leads to molecularly ordered interfaces on TiO<sub>2</sub> in air and solution. *Science* **2018**, *361*, 786–789.
- (77) Khare, P.; Kumar, N.; Kumari, K. M.; Srivastava, S. S. Atmospheric formic and acetic acids: An overview. *Rev. Geophys.* **1999**, *37*, 227–248.
- (78) Grinter, D. C.; Nicotra, M.; Thornton, G. Acetic Acid Adsorption on Anatase TiO<sub>2</sub>(101). *J. Phys. Chem. C* **2012**, *116*, 11643–11651.
- (79) Chen, L.; Kovarik, L.; Szanyi, J. Temperature-Dependent Communication between Pt/Al<sub>2</sub>O<sub>3</sub> Catalysts and Anatase TiO<sub>2</sub> Dilutant: the Effects of Metal Migration and Carbon Transfer on the Reverse Water–Gas Shift Reaction. *ACS Catal.* **2021**, *11*, 12058–12067.
- (80) Whittaker, T.; Kumar, K. B. S.; Peterson, C.; Pollock, M. N.; Grabow, L. C.; Chandler, B. D. H<sub>2</sub> Oxidation over Supported Au Nanoparticle Catalysts: Evidence for Heterolytic H<sub>2</sub> Activation at the Metal–Support Interface. *J. Am. Chem. Soc.* **2018**, *140*, 16469–16487.
- (81) Panayotov, D. A.; Yates, J. T. Spectroscopic Detection of Hydrogen Atom Spillover from Au Nanoparticles Supported on TiO<sub>2</sub>: Use of Conduction Band Electrons. *J. Phys. Chem. C* **2007**, *111*, 2959–2964.
- (82) Mahdavi-Shakib, A.; Kumar, K. B. S.; Whittaker, T. N.; Xie, T.; Grabow, L. C.; Rioux, R. M.; Chandler, B. D. Kinetics of H<sub>2</sub> Adsorption at the Metal–Support Interface of Au/TiO<sub>2</sub> Catalysts Probed by Broad Background IR Absorbance. *Angew. Chem. Int. Ed.* **2021**, *60*, 7735–7743.
- (83) Wang, X.; Shi, H.; Szanyi, J. Controlling selectivities in CO<sub>2</sub> reduction through mechanistic understanding. *Nat. Comm.* **2017**, *8*, No. 513.
- (84) Wang, X.; Hong, Y.; Shi, H.; Szanyi, J. Kinetic modeling and transient DRIFTS–MS studies of CO<sub>2</sub> methanation over Ru/Al<sub>2</sub>O<sub>3</sub> catalysts. *J. Catal.* **2016**, *343*, 185–195.
- (85) Wang, X.; Shi, H.; Kwak, J. H.; Szanyi, J. Mechanism of CO<sub>2</sub> Hydrogenation on Pd/Al<sub>2</sub>O<sub>3</sub> Catalysts: Kinetics and Transient DRIFTS–MS Studies. *ACS Catal.* **2015**, *5*, 6337–6349.
- (86) Lu, J.; Aydin, C.; Browning, N. D.; Gates, B. C. Oxide- and Zeolite-Supported Isostructural Ir(C<sub>2</sub>H<sub>4</sub>)<sub>2</sub> Complexes: Molecular-

- Level Observations of Electronic Effects of Supports as Ligands. *Langmuir* **2012**, *28*, 12806–12815.
- (87) Lu, J.; Serna, P.; Gates, B. C. Zeolite- and MgO-Supported Molecular Iridium Complexes: Support and Ligand Effects in Catalysis of Ethene Hydrogenation and H–D Exchange in the Conversion of H<sub>2</sub> + D<sub>2</sub>. *ACS Catal.* **2011**, *1*, 1549–1561.
- (88) Babucci, M.; Fang, C.-Y.; Hoffman, A. S.; Bare, S. R.; Gates, B. C.; Uzun, A. Tuning the Selectivity of Single-Site Supported Metal Catalysts with Ionic Liquids. *ACS Catal.* **2017**, *7*, 6969–6972.
- (89) Abdel-Mageed, A. M.; Wiese, K.; Hauble, A.; Bansmann, J.; Rabeah, J.; Parlinska-Wojtan, M.; Brückner, A.; Behm, R. J. Steering the selectivity in CO<sub>2</sub> reduction on highly active Ru/TiO<sub>2</sub> catalysts: Support particle size effects. *J. Catal.* **2021**, *401*, 160–173.
- (90) Chen, S.; Abdel-Mageed, A. M.; Mochizuki, C.; Ishida, T.; Murayama, T.; Rabeah, J.; Parlinska-Wojtan, M.; Brückner, A.; Behm, R. J. Controlling the O-Vacancy Formation and Performance of Au/ZnO Catalysts in CO<sub>2</sub> Reduction to Methanol by the ZnO Particle Size. *ACS Catal.* **2021**, *11*, 9022–9033.
- (91) Abdel-Mageed, A. M.; Klyushin, A.; Rezvani, A.; Knop-Gericke, A.; Schlägl, R.; Behm, R. J. Negative Charging of Au Nanoparticles during Methanol Synthesis from CO<sub>2</sub>/H<sub>2</sub> on a Au/ZnO Catalyst: Insights from Operando IR and Near-Ambient-Pressure XPS and XAS Measurements. *Angew. Chem., Int. Ed.* **2019**, *58*, 10325–10329.
- (92) Abdel-Mageed, A. M.; Klyushin, A.; Knop-Gericke, A.; Schlägl, R.; Behm, R. J. Influence of CO on the Activation, O-Vacancy Formation, and Performance of Au/ZnO Catalysts in CO<sub>2</sub> Hydrogenation to Methanol. *J. Phys. Chem. Lett.* **2019**, *10*, 3645–3653.
- (93) Wang, Y.; Widmann, D.; Behm, R. J. Influence of TiO<sub>2</sub> Bulk Defects on CO Adsorption and CO Oxidation on Au/TiO<sub>2</sub>: Electronic Metal–Support Interactions (EMSI) in Supported Au Catalysts. *ACS Catal.* **2017**, *7*, 2339–2345.
- (94) Kelly, S. D.; Charochak, M. E.; Blackwell, N.; Bare, S. R. EXAFS Model of 2-Dimensional Platinum Clusters. *J. Phys.: Conf. Ser.* **2013**, *430*, No. 012061.
- (95) Cuanya, B. R.; Origoza, M. A.; Ono, L. K.; Behafarid, F.; Mostafa, S.; Croy, J. R.; Paredis, K.; Shafai, G.; Rahman, T. S.; Li, L.; et al. Thermodynamic properties of Pt nanoparticles: Size, shape, support, and adsorbate effects. *Phys. Rev. B* **2011**, *84*, No. 245438.
- (96) Chen, L.; Meyer, L. C.; Kovarik, L.; Meira, D.; Pereira-Hernandez, X. I.; Shi, H.; Khivantsev, K.; Gutiérrez, O. Y.; Szanyi, J. Disordered, Sub-Nanometer Ru Structures on CeO<sub>2</sub> are Highly Efficient and Selective Catalysts in Polymer Upcycling by Hydrogenolysis. *ACS Catal.* **2022**, *12*, 4618–4627.
- (97) Shao, X.; Prada, S.; Giordano, L.; Pacchioni, G.; Nilius, N.; Freund, H.-J. Tailoring the Shape of Metal Ad-Particles by Doping the Oxide Support. *Angew. Chem., Int. Ed.* **2011**, *50*, 11525–11527.
- (98) Risso, T.; Shaikhutdinov, S.; Nilius, N.; Sterrer, M.; Freund, H.-J. Gold Supported on Thin Oxide Films: From Single Atoms to Nanoparticles. *Acc. Chem. Res.* **2008**, *41*, 949–956.
- (99) Sterrer, M.; Risso, T.; Heyde, M.; Rust, H.-P.; Freund, H.-J. Crossover from Three-Dimensional to Two-Dimensional Geometries of Au Nanostructures on Thin MgO(001) Films: A Confirmation of Theoretical Predictions. *Phys. Rev. Lett.* **2007**, *98*, No. 206103.
- (100) Lemire, C.; Meyer, R.; Shaikhutdinov, S. K.; Freund, H. J. CO adsorption on oxide supported gold: from small clusters to monolayer islands and three-dimensional nanoparticles. *Surf. Sci.* **2004**, *552*, 27–34.
- (101) Kwak, J. H.; Hu, J.; Mei, D.; Yi, C.-W.; Kim, D. H.; Peden, C. H. F.; Allard, L. F.; Szanyi, J. Coordinatively Unsaturated Al<sup>3+</sup> Centers as Binding Sites for Active Catalyst Phases of Platinum on γ-Al<sub>2</sub>O<sub>3</sub>. *Science* **2009**, *325*, 1670–1673.
- (102) Scheiber, P.; Fidler, M.; Dulub, O.; Schmid, M.; Diebold, U.; Hou, W.; Aschauer, U.; Selloni, A. (Sub)Surface Mobility of Oxygen Vacancies at the TiO<sub>2</sub> Anatase (101) Surface. *Phys. Rev. Lett.* **2012**, *109*, No. 136103.
- (103) Alghannam, A.; Muhich, C. L.; Musgrave, C. B. Adatom surface diffusion of catalytic metals on the anatase TiO<sub>2</sub>(101) surface. *Phys. Chem. Chem. Phys.* **2017**, *19*, 4541–4552.
- (104) Han, Y.; Liu, C.-j.; Ge, Q. Effect of Surface Oxygen Vacancy on Pt Cluster Adsorption and Growth on the Defective Anatase TiO<sub>2</sub>(101) Surface. *J. Phys. Chem. C* **2007**, *111*, 16397–16404.